GEOCHRONOMETRIA 53 (2026) 221620
DOI 10.20858/geochr/221620

Available online at https://www.geochronometria.com/

METHODOLOGICAL ADVANCES AND REMAINING LIMITATIONS IN LUMINESCENCE DATING OF FLUVIAL CLASTS FROM GRAVELLY ALLUVIAL TERRACES OF THE BRUCHE RIVER, NE. FRANCE

MADHURIMA MARIK[1], ELENA SERRA[1, 2], STEPHAN OPITZ[3], DOMINIC WOELKI[1], GILLES RIXHON[4] and FRANK PREUSSER[1]

[1]Institute of Earth and Environmental Sciences, University of Freiburg, Albertstraße 23b, 79104 Freiburg, Germany
[2]Institute of Earth Surface Dynamics, University of Lausanne, Bâtiment Géopolis, Rue de la Mouline 11, 1015 Lausanne, Switzerland
[3]Institute of Geography, University of Cologne, Zülpicher Straße 45, 50674 Cologne, Germany
[4]Faculty of Geography and Planning, University of Strasbourg, UMR LIVE 7362-CNRS-UNISTRA-ENGEES, 67083 Strasbourg, France

Received 28 November 2025 Accepted 8 May 2026

Abstract
Rock surface luminescence dating has developed into a promising approach to constrain depositional ages of clasts. The prerequisites for its successful application are the precise determination of the clast-specific dosimetry and the sufficient pre-burial resetting of the luminescence signal into a certain depth beneath the clast-surface. Dosimetry of clasts is significantly influenced by the internal beta dose rate, which largely depends on grain-size range and internal potassium content of feldspar within rock slices. In the current study, six clasts are investigated from three distinct fluvial terraces of the Bruche River in north-eastern France. Previously published independent age control from sandy deposits of the terraces indicate depositional ages of ~12–14 ka for the youngest, ~27–35 ka for the middle, and a minimum age of ~200 ka for the oldest terrace. Clast-based multi-elevated-temperature post-IR infrared stimulated luminescence (pIR) ages show systematic deviations from age control, overestimating by ~50–150% for the youngest terrace, ~10–30% for the middle terrace, but confirming the minimum age for the oldest terrace. The present study provides methodological advancements by estimating grain-size range and K-content in feldspar grains within rock slices using µ-X-ray fluorescence and microprobe analysis, respectively. Modern clasts from the present riverbed indicate that high-temperature pIR signals retain significant residual ages in rock slices, ranging from ~2–3 ka for pIR_{110} over ~5–6 ka for pIR_{170} to ~8 ka for pIR_{225} signals, while IR_{50} residual ages remain negligible (<1 ka). This study also demonstrates the potential for using fully saturated rock slices from clast interiors to perform reliable fading correction. As the clast-based luminescence ages overestimate the corresponding ages derived from sandy deposits, this highlights the remaining limitations that must be considered for this approach.

Keywords
Luminescence dating, clast dosimetry, modern clasts, residual signal, anomalous fading

1. Introduction

Luminescence dating has emerged as a promising geochronological tool in the past few decades to determine numerical ages of fluvial sediment deposition. Traditionally, sediment grain size of <0.5 mm is used in this method (Wintle, 1997), which requires the presence of sand lenses within the investigated stratigraphy. However, sand lenses may be sparse in many proximal fluvial and glaciofluvial deposits, thereby limiting the applicability of luminescence dating. Recent studies have, therefore, explored the potential of applying luminescence to date the rock surfaces of clasts (Ageby *et al*., 2021; Ishii, 2024; Jenkins *et al*., 2018; Kenworthy *et al*., 2014; Marik *et al*., 2024; Rades *et al*., 2018; Sohbati *et al*., 2011). Prolonged daylight exposure can reset the latent luminescence signal to a

Corresponding author: M. Marik
e-mail: madhurima.marik@geologie.uni-freiburg.de

ISSN 1897-1695 (online), 1733-8387 (print)

measurable depth beneath clast-surface, giving origin to luminescence-depth profiles which remain preserved following burial within completely bleached clasts (*e.g.* Sohbati *et al*., 2011). Unlike sand or silt-sized grains, clasts can, therefore, retain a record of their pre-burial bleaching history, offering significant advantages for reconstructing depositional ages.

Despite recent advancements, rock surface luminescence dating remains subject to key challenges. First, calculating the environmental dose rate from clasts requires quantifying (i) the grain size distributions of K-feldspar and (ii) the percentage of internal potassium concentration (K_{int}) of K-feldspar within rock slices. In previous studies, K-feldspar grain-size range within rock slices was assessed either using μ-X ray fluorescence (XRF) elemental mapping and delineating possible K-feldspar grains (Ishii *et al.*, 2022; Liu *et al*., 2022; Rades *et al*., 2018) or using petrographic observations of clast-thin sections (Ageby *et al*., 2023; Marik *et al*., 2024; Serra *et al*., 2025). However, considering the heterogeneous distribution of K-feldspar grains within a rock slice, no standardized or widely accepted procedure exists to this day for deriving the ideal grain-size range of K-feldspar. Besides, earlier studies (Ishii *et al.*, 2022; Jenkins *et al*., 2018) have mostly relied on a generalised assumption of 12.5 ± 0.5% (Huntley and Baril, 1997) or 10 ± 2% (Smedley *et al*., 2012) for K_{int} while determining clast dosimetry. Both factors introduce significant uncertainty to the dose rate estimation from clasts.

Second, while fluvial sand grains are typically transported over long distance with sufficient daylight exposure, fluvial clasts are transported over smaller distances along the riverbed and are less likely to be fully bleached before burial (Ishii *et al*., 2022). This raises concerns about partial bleaching of clasts, leading to age overestimation (Wallinga, 2002). Assessing residual luminescence signals in modern clasts is therefore essential to evaluate the extent of incomplete bleaching. Although modern sand samples from a range of water-laid environments have been extensively studied to evaluate signal resetting in older sandy deposits (Marik *et al*., 2025; Chamberlain and Wallinga, 2019; Jain *et al*., 2004), relatively few investigations have focused to study contemporary clasts from modern fluvial systems (Liu *et al*., 2019; Liu *et al*., 2023). This is likely because modern clasts commonly experience limited bleaching during transport and deposition, reducing their suitability for determining reliable luminescence age. Luminescence dating of modern clasts, however, offers direct insights into the extent of signal resetting, identifying the presence of residual signals within the clasts obtained from older deposits.

Third, while quartz is usually preferred over feldspar in conventional sediment dating because of its better bleachability, its application in rock surface luminescence dating is limited. Quartz in bedrock slices often yields very dim Optically Stimulated Luminescence (OSL) signals that are unsuitable for dating applications (*e.g.*, Preusser *et al*., 2006; Sohbati *et al*., 2011; Ishii *et al*., 2022). In addition, quartz is sensitive primarily to short wavelengths (UV) rather than infrared, meaning that quartz grains at greater depths are not easily bleached due to light attenuation resulting in very shallow luminescence depth profiles (Singareyer and Bailey, 2004). Moreover, unlike sand-sized grains, where mineral separation can be performed, slices from clasts do not undergo density separation procedure. Therefore, unless the clast is purely quartzite, its OSL signal is unavoidably contaminated by feldspars.

The above limitations have led researchers to target K-rich feldspar grains present within the rock slices despite the fact that luminescence signals from feldspar grains commonly suffer from anomalous fading (Wintle, 1973, 1977), *i.e.* signal loss with time that causes age underestimation. To correct the underestimated ages derived from the rock slices, two methods have been commonly used within recent rock surface luminescence studies. In the first and conventional approach, the rate of luminescence signal loss is quantified via controlled storage experiments, in which feldspar grains within rock slices are measured at defined time intervals to characterize their fading behaviour. From this, the fading rate (g-value, %/decade) is estimated and used for fading correction (Auclair *et al*., 2003; Huntley and Lamothe, 2001). The second approach for fading correction is based on measuring natural to laboratory saturation (NLS) ratios (Rades *et al*., 2018) by comparing the luminescence signals of naturally saturated slices (*i.e.* deep within the clast) with those of laboratory-saturated (*i.e.* irradiated) slices. When fading is absent, these two signals should be identical, while any difference between them represents the presence of fading (Rades *et al*., 2018; Rades *et al*., 2024). Following the later approach, fading-corrected ages are calculated by dividing the faded ages by the NLS ratio. The fading correction procedure using the NLS ratio potentially reduces the uncertainties associated with the conventional g-value calculation, thereby improving the reliability of fading-corrected depositional ages from clasts (Rades *et al*., 2018). This approach is also faster than the conventional storage tests which may take several days to measure each rock slice. Previous cobble studies (Liu *et al*., 2019; Liu *et al*., 2023) have also tried to mitigate the phenomenon of anomalous fading by using the Multi-Elevated Temperature post-Infrared (MET-pIRIR) protocol, where luminescence signals are measured at progressively higher IR stimulation temperature (Li and Li, 2011). However, while high temperature pIRIR signals exhibit lower fading rates, these signals are hard to bleach by natural daylight (Liu *et al*., 2019).

The points raised above highlight the need of further refining the clast luminescence dating method to enable its application as a reliable dating method. In the present study, fluvial clasts collected from three distinct fluvial terraces of the Bruche River in north-eastern France (**Fig. 1a**) are analysed and dated with the MET-pIRIR protocol (Li and Li, 2011). This setting was chosen because independent age control is available, allowing us to critically assess

the performance and reliability of the clast-based luminescence ages. Our study precisely estimates the dosimetry of the clasts and attempts to mitigate the problem of anomalous fading in K-feldspar grains within the rock slices. Alongside, modern clasts retrieved directly from the riverbed are examined to quantify residual doses within older clasts, particularly at high temperature pIRIR signals. Resulting depositional ages derived from the clasts are compared with quartz OSL and feldspar MET-pIRIR ages obtained from sand layers and matrix sediments from the corresponding terraces (Marik *et al*., 2025). In summary, the current study reports a detailed methodological framework for luminescence dating of K-feldspar-bearing clasts and provides new insights into its applicability and accuracy, addressing its limitations in complex fluvial depositional environments.

2. Regional Setting

Located in north-eastern France, the ~80 km long Alsatian Bruche River flows into the Ill River directly upstream of the city of Strasbourg (**Fig. 1a**-**1b**). It is one of the main western sub-tributaries of the Upper Rhine owing to its ~730 km^2 large catchment and has a mean longitudinal slope of ~0.007 m/m (Jautzy *et al*., 2022). Geological and geomorphological characteristics of the catchment allow distinguishing between two main river sections. The ~50 km upper reach flows from the source, located at ~690 m above sea level (a.s.l.) through the northernmost crystalline Vosges Mountains, to roughly Molsheim (**Fig. 1b**). The ~30 km long lower section (*i.e.* from Molsheim to the confluence with the Ill, **Fig. 1b**) successively drains the Vosgian footslopes and part of the Upper Rhine Graben (URG), where the width of the floodplain locally exceeds 1 km (**Fig. 1c**). Among the large rivers draining the southwestern part of the URG and developing km-wide alluvial fans in this long-term subsiding area (*e.g.* Fecht, Giessen/Liepvrette, Thur, Zorn), the Bruche system clearly stands out (Maire, 1966; Wuscher, 2021). Its Quaternary alluvial formations are the only ones to be found at topographically higher-lying positions in the landscape and thereby form several terraces flanking its lower valley (**Fig. 1c**; Baulig, 1922; Castela and Tricart, 1958; Lautridou *et al*., 1985; Théobald, 1955). Four distinct levels of fan-like terrace deposits (hereinafter labelled as T1-T4, from highest to lowest; **Fig. 1c**) are identified by Maire (1966). The subsurface databases of the French Geological Survey (BRGM: https://infoterre.brgm.fr/viewer/MainTileForward.do) provide information on drillings performed in these terraces close to each sampling site. This data reveals that the thickness of alluvial bodies exceeds 50 m in T1, T3 and T4 . Although loamy/sandy layers are present, the stratigraphy is predominantly gravel-supported. In T4, ~2.6 m high fining upward sequence evolves from clast and sand-supported layers at the base to silty/loamy material at the top (**Fig. 2a**). Within T3, clast-supported units dominate the ~5 m sediment exposure, where clasts are interbedded with coarse grained matrix and sand lenses (**Fig. 2b**). T1 exhibits at least 6 m of fluvial deposits, that are overlain by a 1.5–2 m thick loess cover. Although clast-supported layers are less common in T1 than in T3 and T4, a well-defined coarse gravel horizon occurs at approximately 8 m below the topographic surface (**Fig. 2c**). Until recently, the chronology of terrace formation remained poorly defined. Marik *et al*. (2025) addressed this issue by applying a combined luminescence dating approach to both sand lenses and sandy matrix of the gravel layers. The results indicate depositional ages of ~12–14 ka for the lowest terrace (T4), ~27–35 ka for the lower intermediate terrace (T3), and a minimum age of ~200 ka for the highest terrace (T1).

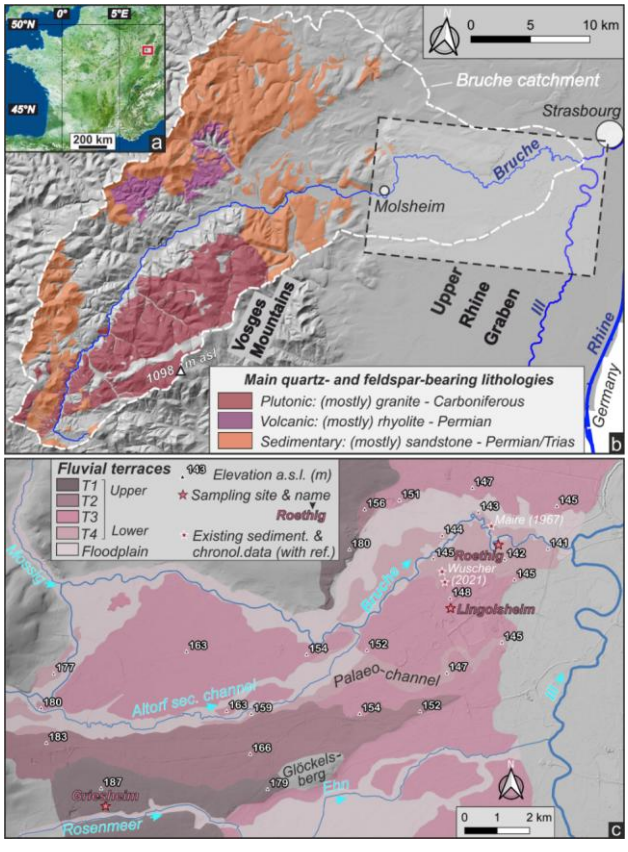

Fig. 1. *(a) Location of the study area in north-eastern France. (b) Simplified lithological map of the Bruche catchment draining the Vosges Mountains and the Upper Rhine Graben. The dashed rectangle in the lower section of the river delimits the study area presented in panel c. (c) Geomorphological map of the lower Bruche showing both terrace (T4 to T1) and floodplain extension (modified from Maire, 1966). Stars with white and red borders refer to the existing sedimentological and/or chronological data in the area and sampled terrace deposits in this study, respectively.*

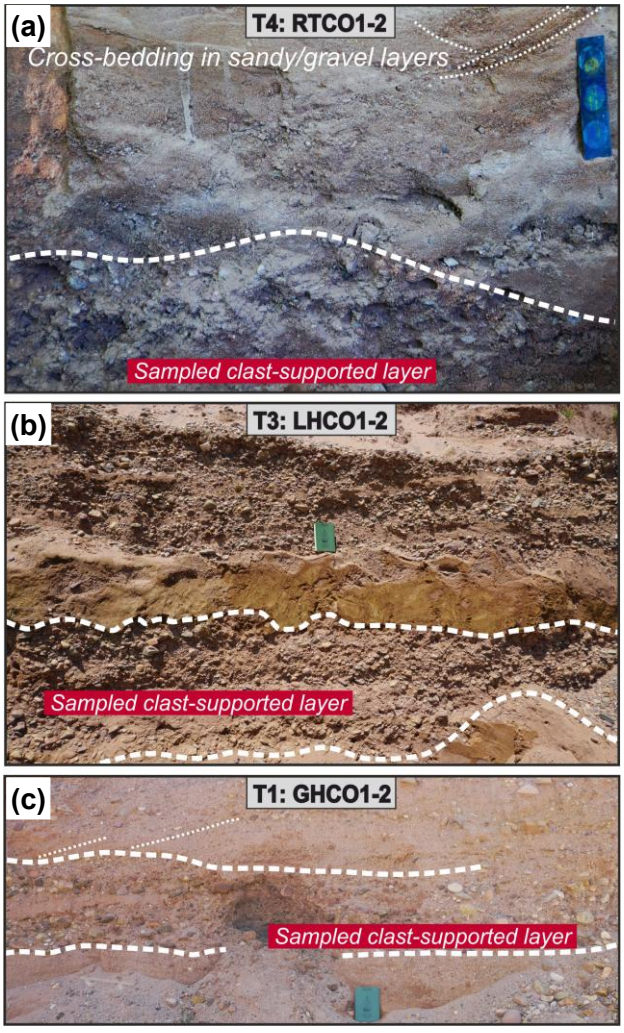

Fig. 2. *Field photographs (G. Rixhon) showing the location of clast sampling within gravel-supported layers of the (a) Roethig terrace (T4), where cross-bedding is present within the sandy/gravelly deposits (measuring tape is 15 cm high); (b) Lingolsheim terrace (T3), where fine-grained horizons are interbedded with clast-supported units, exhibiting cryoturbation features (field book is 12.5 cm high) and (c) Griesheim terrace (T1), where gravelly layer is overlain and underlain by sandy deposits (field book is 12.5 cm high).*

3. Methods

3.1. Field Strategy

Three fluvial terraces of the Bruche River, *i.e.* T4, T3 and T1, are investigated at the sampling sites of Roethig, Lingolsheim, and Griesheim, respectively (**Fig. 1b**). Owing to ongoing lateral channel erosion, samples were collected from a natural exposure of the lowermost terrace (Roethig: 48.569087°N, 7.680825°E, **Fig. 2a**). Two gravel pits were sampled for T3 (Lingolsheim: 48.552341°N, 7.660434°E; **Fig. 2b**) and T1 (Griesheim: 48.502610°N, 7.513700°E; **Fig. 2c**). Sampling of T2 was not possible due to the absence of suitable exposures. Approximately 10–12 rounded to sub-rounded clasts with a maximum diameter varying between ~5–7 cm were collected for luminescence dating from gravel-rich horizons identified within the three terraces. Clasts were retrieved underneath an opaque pond liner (~1 mm thick) covering an area of approximately 3 m^2. The outer, light-exposed layer of the outcrop was first removed, and depositional orientation of selected clast was recorded (*i.e.* to distinguish their top and bottom surfaces) using a red LED head lamp, before storing the clasts in light-safe bags for transport. From the Roethig terrace, clasts (RTCO) were collected from a gravelly matrix dominated layer at a depth of ~2.5 m below the topographic surface (**Fig. 2a**). In the Lingolsheim gravel pit, clasts (LHCO) were obtained at a depth of ~2 m from the visible top of the *in situ* alluvial deposits from a gravel-rich layer (**Fig. 2b**). At the gravel pit of Griesheim, clasts (GHCO) were retrieved from a coarse gravel horizon at a depth of ~8 m below the topographic surface (**Fig. 2c**). In addition to the clasts obtained from these three terraces, modern clasts (MODCO) were sampled from the present-day riverbed of the Bruche River, directly downstream of the Roethig outcrop. Modern clasts were collected directly from the exposed surface of the active riverbed, ensuring that their measured residual signals represent the luminescence signals remaining after natural daylight exposure under present-day fluvial conditions. Observation of the clasts' thin sections revealed that one clast from the Roethig terrace (RTCO2) is a sandstone, while the modern clasts and all the other clasts from the Roethig (T4), Lingolsheim (T3) and Griesheim (T1) terraces represent both fine- and coarse-grained granites (**Fig. S1**).

3.2. Sample Preparation and Luminescence Measurements

Clast samples were prepared for luminescence measurements under subdued red light at the luminescence laboratory of the University of Freiburg. Each clast was drilled using a water-cooled diamond-tipped core drill to a varying depth of ~12–15 cm from both the top and bottom clast surfaces, and three to four cores per clast were recovered. Each resulting core was then sliced into ~0.7–0.8 mm thick rock slices using a Buehler Isomet water-cooled diamond-edged saw, with a blade thickness of ~0.3 mm. The cores were relatively fragile and frequent breakages occurred during slicing the cores. In such cases, broken slices were used instead of intact slices during luminescence measurements.

Luminescence measurements of the rock slices were carried out using a Risø TL/OSL DA-20 reader (Bøtter-Jensen *et al.*, 2010) equipped with LED having a peak emission of 870 nm. The $^{90}Sr/^{90}Y$ beta sources used for irradiation was calibrated with the Freiberg-Lexcal 2014 quartz (90–160 µm; Richter *et al.*, 2020) mounted on 2-mm aliquots (dose rate of ~0.10 Gy s^{-1}). It is acknowledged that the dose rate absorbed by the rock slices may be lower (~ 18%) compared to that calibrated for sand grain aliquots (Jenkins *et al.*, 2018). Additional analyses show that

recalculated clast ages using an 18% lower beta dose rate remain consistent with the original clast ages within uncertainty (**Table S2**). Therefore, no correction for this discrepancy was applied, since this factor is highly sample-specific, and applying a generalized correction of ages based on the factor would be less reliable. Furthermore, the rock slices analysed in this study exhibit variable thicknesses and geometries. Because beta attenuation depends strongly on these parameters (Ou *et al*., 2022), calibration using quartzite slice of similar thickness may not adequately represent the absorbed beta dose for all investigated slices. Establishing reliable correction factors would, therefore, require dedicated calibration experiments using rock slices with varying geometries and lithologies. Such calibration efforts remain a methodological gap in the present study and should be addressed in future work to further refine clast dosimetry. Slices were mounted directly on aluminium cups with silicon oil and their infrared (870 nm, ~130 mW/cm^2) stimulated luminescence signal (IRSL) was detected through a 2 mm Schott BG-39 and a 3 mm Schott BG-3 filter combination. From each rock slice, equivalent dose (D_e) value was determined with MET-pIRIR protocol (Table 1), where, in addition to measuring the IR_{50} signal, high temperature pIRIR signals at pIR_{110}, pIR_{170} and pIR_{225} were measured with the aim of targeting IRSL signals with ideally negligible fading (Fu and Li, 2013; Li and Li, 2011). Signals from test doses (~10 Gy) were used for correcting the sensitivity changes in the MET-pIRIR protocol and a low heating rate of 2°C s^{-1} was maintained during the measurements to avoid any thermal offset (Elkadi *et al*., 2021; Jenkins *et al*., 2018). Through additional dose recovery experiments using larger test doses (>10 Gy), it has been observed that increasing the test dose resulted in an abrupt increase in sensitivity, particularly after the first measurement cycle. Therefore, a constant test dose of ~10 Gy was adopted to ensure stable sensitivity correction during MET-pIRIR measurements across all rock slices. A preheat temperature of 250°C for 60 s was used in the protocol and an additional 30 s pause and 100 s pause were incorporated before IR_{50}/pIR_{110} and pIR_{170}/pIR_{225} stimulations, respectively. The longer pause at higher stimulation temperatures allows sufficient time for thermal stabilization of the discs/slices, as demonstrated in previous studies (Fu *et al*., 2012; Jenkins *et al*., 2018; Liu *et al*., 2022). For D_e determination, signals were integrated over the first 15 s of stimulation, and a late background subtraction was applied using the last 30 s. Dose response curves were fitted with an exponential plus linear function. Routine rejection criteria were followed to accept the D_e values derived from the rock slices, with a recycling ratio of 10% and a recuperation <10% of the natural dose. Although this study explicitly targets the outermost slices for depositional age calculation from corresponding clast (section 4.2), the application of these rejection criteria influences the number of accepted D_e values and thus the final age estimates. While the impact of this criterion is minimal for the Roethig terrace clasts, it becomes more pronounced for the Lingolsheim and especially the Griesheim terrace clasts, where a larger number of outermost slices do not meet the criteria. Consequently, the number of retained slices varies between clasts, affecting the CAM-based age estimates from the outermost slices. This impact is observed to be minor at lower IR stimulation temperatures (*e.g.*, IR_{50} and pIR_{110}), but increases at higher stimulation temperatures (*e.g.*, pIR_{170} and pIR_{225}).To verify the reliability of the applied MET-pIRIR protocol, dose recovery tests were conducted on bleached rock slices. Four clasts from each river terrace along with four modern riverbed clasts were utilized for dose recovery tests. Three inner slices from each clast were bleached for 300 s at 225°C in three consecutive steps under blue LEDs within the Risø reader. Two clasts from each river terrace and two clasts among the modern riverbed clasts recovered doses within 10% of unity for all MET-pIRIR signals and were, therefore, used for D_e determination (**Fig. 3**). The other clasts showed larger scatter within dose recovery tests, possibly reflecting variable signal sensitivity and/or lithological differences (Tissoux *et al.,* 2026). Although pre-bleaching before dose recovery tests at high temperature (225°C) may potentially induce sensitivity changes, these were compensated for by the sensitivity correction inherent to the SAR protocol through test-dose normalization after each regenerative cycle. Furthermore, the residual signal after bleaching was <3% of the given dose and was considered negligible. Therefore, no additional residual dose correction was applied in the dose recovery calculations.

To determine anomalous fading related to the MET-pIRIR signals of the investigated clasts, NLS ratios (Rades *et al*., 2018) was estimated for each clast. The NLS ratio was calculated by dividing the natural saturation (L_n/T_n) from the deepest or central most slice of each core (*i.e.* the slices that are assumed to be unaffected by pre-burial sunlight exposure). The laboratory saturation (L_{sat}/N_{sat}) was measured on that specific slice by providing the radiation dose of 5000 Gy (**Fig. 4**). NLS ratio was estimated for each

Table 1. *MET-pIRIR protocol modified after Li and Li (2011) used here to date individual rock 290 slices from the investigated clasts.*

step	Modified MET-pIRIR protocol
1	Natural or regenerative dose
2	Preheat at 250°C for 60 s
3	IR stimulation at 50°C for 100 s
4	IR stimulation at 110°C for 100 s
5	IR stimulation at 170°C for 100 s
6	IR stimulation at 225°C for 100 s
7	Test dose, D_t
8	Preheat at 250°C for 60 s
9	IR stimulation at 50°C for 100 s
10	IR stimulation at 110°C for 100 s
11	IR stimulation at 170°C for 100 s
12	IR stimulation at 225°C for 100 s
13	Return to step 1

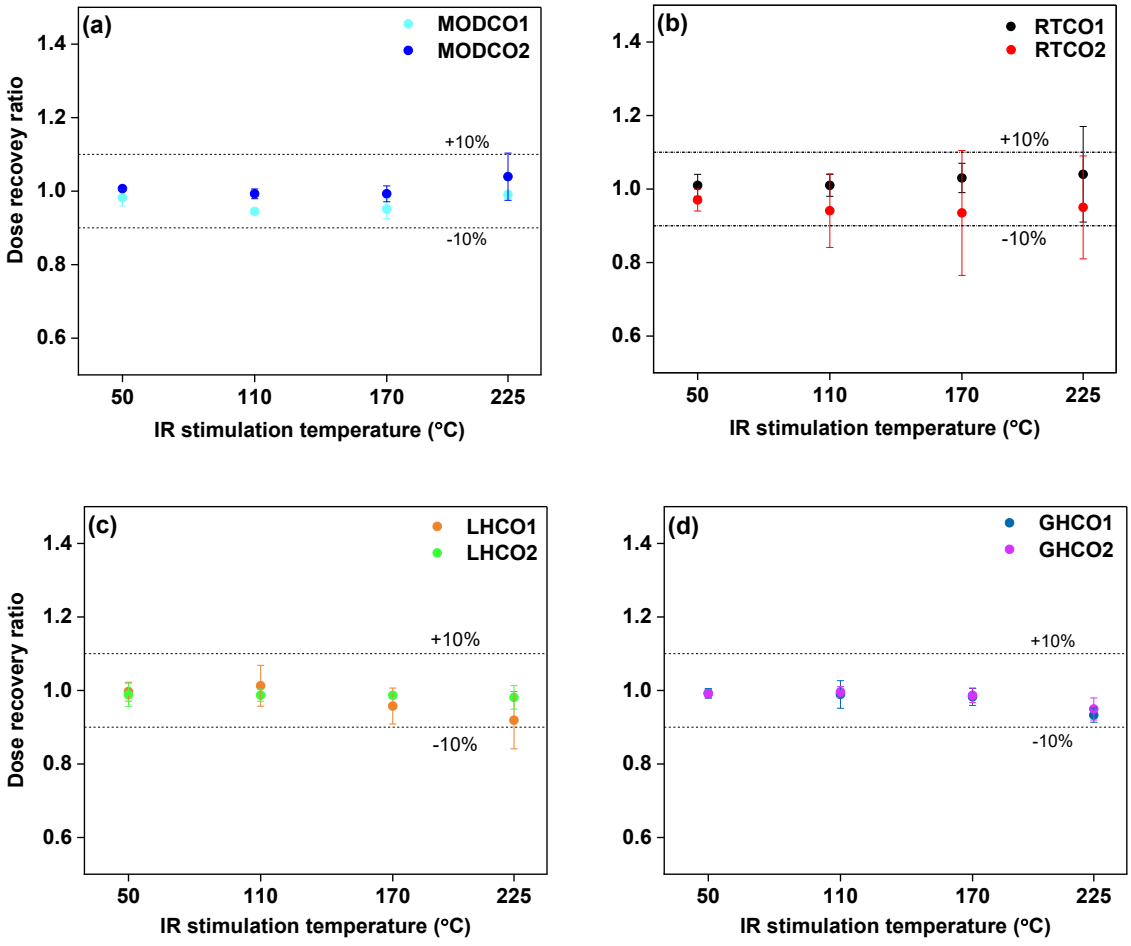

Fig. 3. *Dose recovery test results on clasts obtained from (a) modern riverbed, (b) Roethig, (c) Lingolsheim and (d) Griesheim terrace. Each data point represents the mean dose recovery ratio obtained from 3 inner slices per clast. Corresponding error bars indicate the standard deviation.*

clast, by averaging the NLS ratio obtained from three central rock slices.

3.3. Dose Rate Determination

Approximately 200 g of gravelly matrix material surrounding the clasts were collected from the investigated terraces to measure the concentration of radioelements (K, Th and U) using high-resolution gamma spectrometry (Preusser *et al.*, 2023). Both the individual clasts and the clast-surrounding matrix sediments (<2 mm) were crushed and milled. Gamma spectrometry was then performed at the University of Freiburg after one month of storage to build up radioactive equilibrium between radon and its daughter isotopes in the samples; no evidence for radioactive disequilibrium was observed in the Uranium decay chain. The dose rate of individual rock slices was estimated with the *calc_CobbleDoseRate()* R function (Riedesel and Autzen, 2023), which integrates the attenuated beta and gamma dose rate profiles within the clast based on the radioelement concentrations measured on the clast and on the clast surrounding matrix sediments, using the attenuation factors modelled by Riedesel and Autzen (2020). A Depth-independent alpha efficiency factor (a-value) of 0.05 ± 0.01 (Preusser, 1999) was assumed for the feldspar grains within the clasts. A water content of 10 ± 5% was assumed for the clast-surrounding matrix, while the moisture content within the clasts was assumed negligible. A long-term average moisture content was assumed for sandy matrix sediments (Marik *et al.*, 2024, 2025; Roskosch *et al.*, 2015). Actual moisture content measurement values were not considered since they might not reflect burial conditions over geological timescales (Degering and Degering, 2020). Internal beta radiation was estimated based on the grain size and the internal K% (K_{int}) of the K-feldspar grains within the clasts. To determine the K_{int}, the major and minor element compositions of K-feldspars were measured on thin sections of each investigated clast, using a JEOL JXA iHP 200F electron microprobe analyser (EMPA) at the University of Freiburg. All elements were calibrated against natural and synthetic, well-characterised mineral reference materials. An accelerating voltage of 15 kV was used throughout the course of the measurement. The feldspars were analysed with 15 nA beam current, a counting times of 20 s on the peak

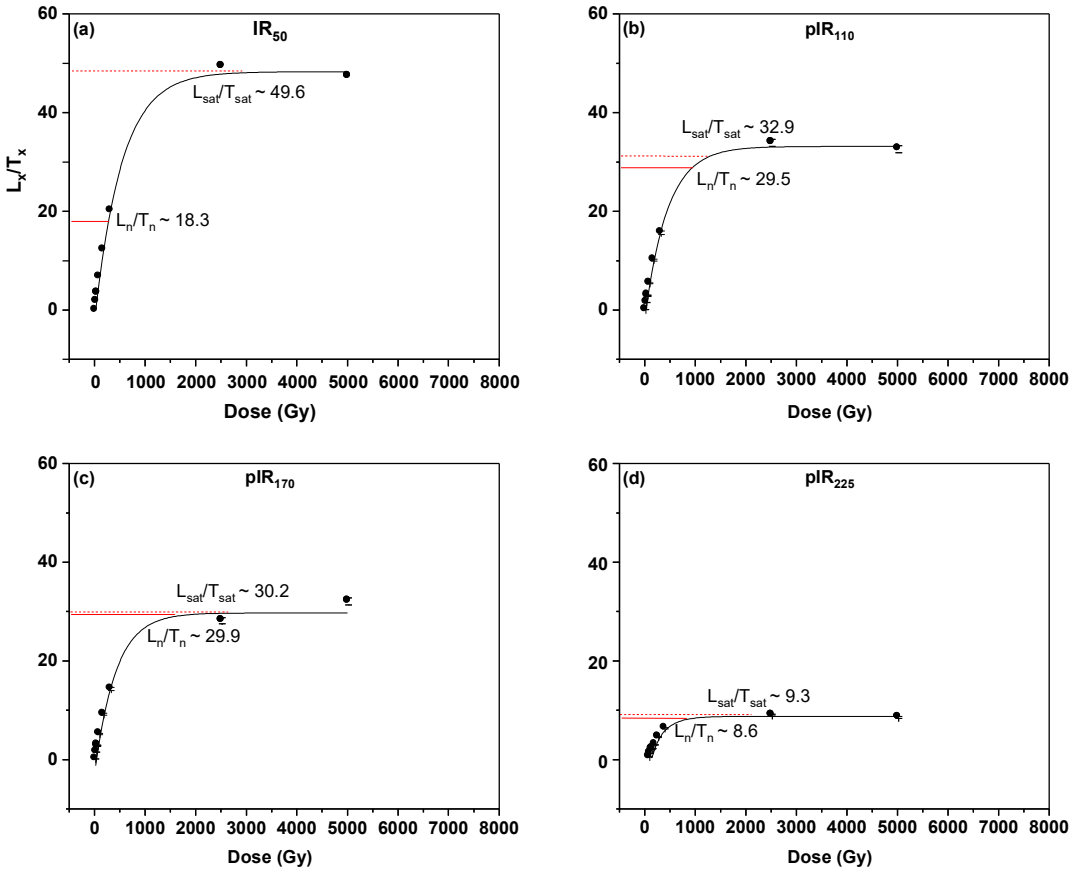

Fig. 4. *Dose response curves (DRC) fitted with exponential function for (a) IR_{50}, (b) pIR_{110}, (c) pIR_{170} and (d) pIR_{225}, shown for one representative rock slice obtained from the centre of clast sample RTCO1. Laboratory saturation signals are measured at 5000 Gy to interpret the NLS ratio (i.e. $(L_n/T_n)/(L_{sat}/N_{sat})$) for fading correction and the DRCs show the variation in saturation behaviour across different IR stimulation temperatures. The solid horizontal line marks the measured natural signal (L_n/T_n) and the dashed horizontal line indicates the corresponding laboratory saturation level (L_{sat}/N_{sat}).*

and 10 s on the background with a spot size, set to 2 µm. A set of in-house silicate standards were regularly measured to check for precision and accuracy. Calibration standards were albite for Si and Na, orthoclase for Al and K, diopside for Ca, and chromite for Fe. The matrix correction factors (ZAF: atomic number, absorption, fluorescence) were applied to all data and relative uncertainties of major element oxides were on the order of 1–2%.

To determine the K-feldspar grain size distribution, one slice from each investigated clast was analysed using an energy-dispersive µ-XRF device (Bruker M4 Tornado) equipped with a rhodium anode, operated at 50 kV and 300 µA, at the University of Cologne. With a beam spot size of 20 µm and a spatial resolution of 35 µm, elemental maps of the sample material were generated. Each measurement point was recorded with an integration time of 100 ms. The analyses were conducted under a controlled vacuum environment maintained at 20 mbar to improve the sensitivity for light elements. Data acquisition was carried out using two detectors, allowing for high-resolution elemental mapping. From the elemental maps, K-rich grains were identified and polygons outlining individual grains were drawn using ImageJ software. K-feldspar grain size was estimated from each polygon using ImageJ. Based on the estimated K-feldspar grain size and K_{int}, the internal beta dose rate contribution were calculated with the ADELEv2017 software (Degering and Degering, 2020). To obtain the total effective dose rate of each rock slice, the internal beta component was added to the cosmic dose rate contribution determined following Prescott and Hutton (1994) and to the external beta and gamma dose rates of each rock slices (Riedesel and Autzen, 2020). Owing to the fragile nature of the cores recovered from clast RTCO1 of the Roethig terrace, no intact slices could be prepared. Although RTCO1 and RTCO2 differ in lithology (section 3.1), microscopic examination of the clasts' thin sections indicated comparable K-feldspar grain sizes (**Fig. S1a** and **S1b**). Consequently, the grain-size estimate derived from RTCO2 was adopted as a proxy for RTCO1.

4. Results

4.1. Dosimetry of Clasts

Fig. 5 shows the grain-size distribution of K-rich feldspar grains within rock slices, estimated using μ-XRF analysis. Across the rock slices investigated, the density distributions of grain sizes are non-unimodal. For each distribution, the interquartile percentage range (*i.e.* from 25th to 75th percentile) was used to define grain-size ranges of K-feldspars within the rock slices (Fig. 5c, 5f, 5i, 5l, 5o) and the resulting effective grain size ranges are summarized in Table 2. An interquartile percentage range represents the dominant grain-size population of K-feldspar within each slice. This approach reduces the influence of very fine or very coarse grains that occupy only limited areas within the slice and are therefore unlikely to contribute significantly to the measured IRSL signal. Based on the results, the effective grain size for RTCO2 is 225–375 μm and a similar grain size range is assumed for RTCO1, as explained in section 3.3. For the Lingolsheim terrace, LHCO1 and LHCO2 have grain size ranges of 275–525 μm and 225–425 μm, respectively. From the Griesheim terrace, GHCO1 and GHCO2 exhibit grain sizes of 325–675 μm and 225–375 μm, respectively.

Microprobe analysis of thin sections from the clasts yields K_{int} values of ~11.6–11.8%, ~13.3–13.6% and 12.9–13.3% for the Roethig, Lingolsheim and Griesheim terraces, respectively. Table 2 reports the effective dose rate values estimated for the surface slice of each clast, based on K_{int}, grain size and radionuclide concentrations measured for the clasts and the surrounding matrix sediments. Clasts from the Roethig terrace (RTCO1 and 2) exhibit relatively low radionuclide concentrations, while higher values were recorded within the clasts investigated from the Lingolsheim (LHCO1 and 2) and the Griesheim (GHCO1 and 2) terraces. LHCO1 displays a much higher thorium content of ~27.2 ppm compared to that exhibited by LHCO2 and the clasts from the Roethig and Griesheim terraces. The total dose rate calculated on the surface slices of the clasts vary between ~2.8 - ~3.0 Gy ka^{-1}, ~5.2 - ~6.0 Gy ka^{-1} and ~4.9 - ~5.0 Gy ka^{-1} for the Roethig, Lingolsheim and the Griesheim terraces, respectively (Table 2). The effective total dose rates derived for the clasts from each terrace are consistent and overlap within 1σ uncertainty, except for the two clasts from the Lingolsheim terrace.

4.2. Luminescence Depth Profiles

Following the initial screening of the clasts by dose recovery tests (Fig. 3, section 3.1), depth-dependent variation in the natural luminescence signals (L_n/T_n) was investigated in six clasts from the terraces (RTCO1, RTCO2, LHCO1, LHCO2, GHCO1 and GHCO2) as well as in two modern-day clasts (MODCO1 and MODCO2). No bottom cores can be retrieved from the other investigated clasts except RTCO1. Hence, the luminescence depth profiles from the clasts are obtained explicitly using the cores obtained from the top surfaces of the clasts. As a consequence, the degree of bleaching could not be assessed in the basal surface of the clasts except RTCO1. Signal normalisation for each core was performed relative to the maximum L_n/T_n value obtained from the corresponding core, where natural luminescence signal is assumed to represent saturation. Considering potential lithological heterogeneity and variability in luminescence signal intensity among slices within the saturation plateau of an individual core, depth profiles are always normalised to the slice exhibiting the maximum L_n/T_n value to define a core-specific saturation level. Sensitivity-corrected L_n/T_n ratios for the IR_{50}, pIR_{110}, pIR_{170} and pIR_{225} signals plotted as a function of depth from the clast surfaces reveal depth-dependent increase in luminescence signals for multiple cores from RTCO1, RTCO2, LHCO1, LHCO2, GHCO1 and GHCO2 (Fig. 6), MODCO1 and 2 (Fig. S2). Visual inspection across the luminescence depth profiles suggests diverse degrees of pre-burial bleaching among different clasts and, for some clasts, differences among cores are observed (Fig. 6 and Fig. S2). Within these profiles, L_n/T_n values are lowest near the surface and gradually increase with depth, approaching saturation towards the clast interior. For multiple cores of RTCO1, RTCO2, LHCO1 and LHCO2, the IR_{50} and pIR_{110} bleaching profiles display a characteristic sigmoidal shape, with a shallow surface-bleaching plateau of L_n/T_n values (Fig. 6), indicating the presence of a pre-

Table 2. *Summary of radionuclide concentrations, internal potassium content (K_{int}) (derived from microprobe analysis) and effective dose rate of the clast surface slices. Grain size range, estimated from the μ-XRF measurement on the rock slice of individual clast sample are indicated. Internal beta dose rates of the rock slices were estimated with the ADELEv2017 software (Degering and Degering, 2020).*

Sample ID	U (ppm)	Th (ppm)	K (%)	Effective grain size range (μm)	Alpha dose rate (Gy ka^{-1})	K_{int} (%)	Int. beta dose rate (Gy ka^{-1})	Gamma dose rate (Gy ka^{-1})	Cosmic dose rate (Gy ka^{-1})	Total dose rate (Gy ka^{-1})
RTCO1	0.48 ± 0.05	1.45 ± 0.18	0.99 ± 0.03	225–375	0.01 ± 0.01	11.8 ± 0.6	1.01 ± 0.05	0.36 ± 0.01	0.10 ± 0.01	2.85 ± 0.17
RTCO2	0.52 ± 0.07	1.47 ± 0.23	1.20 ± 0.03	225–375	0.01 ± 0.01	11.6 ± 0.4	1.00 ± 0.03	0.42 ± 0.02	0.10 ± 0.01	3.02 ± 0.22
LHCO1	1.34 ± 0.14	27.24 ± 1.66	3.48 ± 0.09	275–525	0.05 ± 0.02	13.6 ± 0.3	1.56 ± 0.03	2.30 ± 0.08	0.15 ± 0.02	6.05 ± 0.43
LHCO2	1.97 ± 0.16	10.38 ± 0.76	3.22 ± 0.09	225–425	0.03 ± 0.02	13.3 ± 0.3	1.24 ± 0.03	1.50 ± 0.04	0.15 ± 0.02	5.21 ± 0.35
GHCO1	1.69 ± 0.11	10.31 ± 0.72	2.71 ± 0.07	325–675	0.02 ± 0.01	12.9 ± 0.4	1.84 ± 0.06	1.30 ± 0.04	0.08 ± 0.01	4.95 ± 0.25
GHCO2	1.18 ± 0.12	10.01 ± 0.74	3.52 ± 0.09	225–375	0.03 ± 0.01	13.3 ± 0.4	1.14 ± 0.04	1.50 ± 0.04	0.08 ± 0.01	5.03 ± 0.41

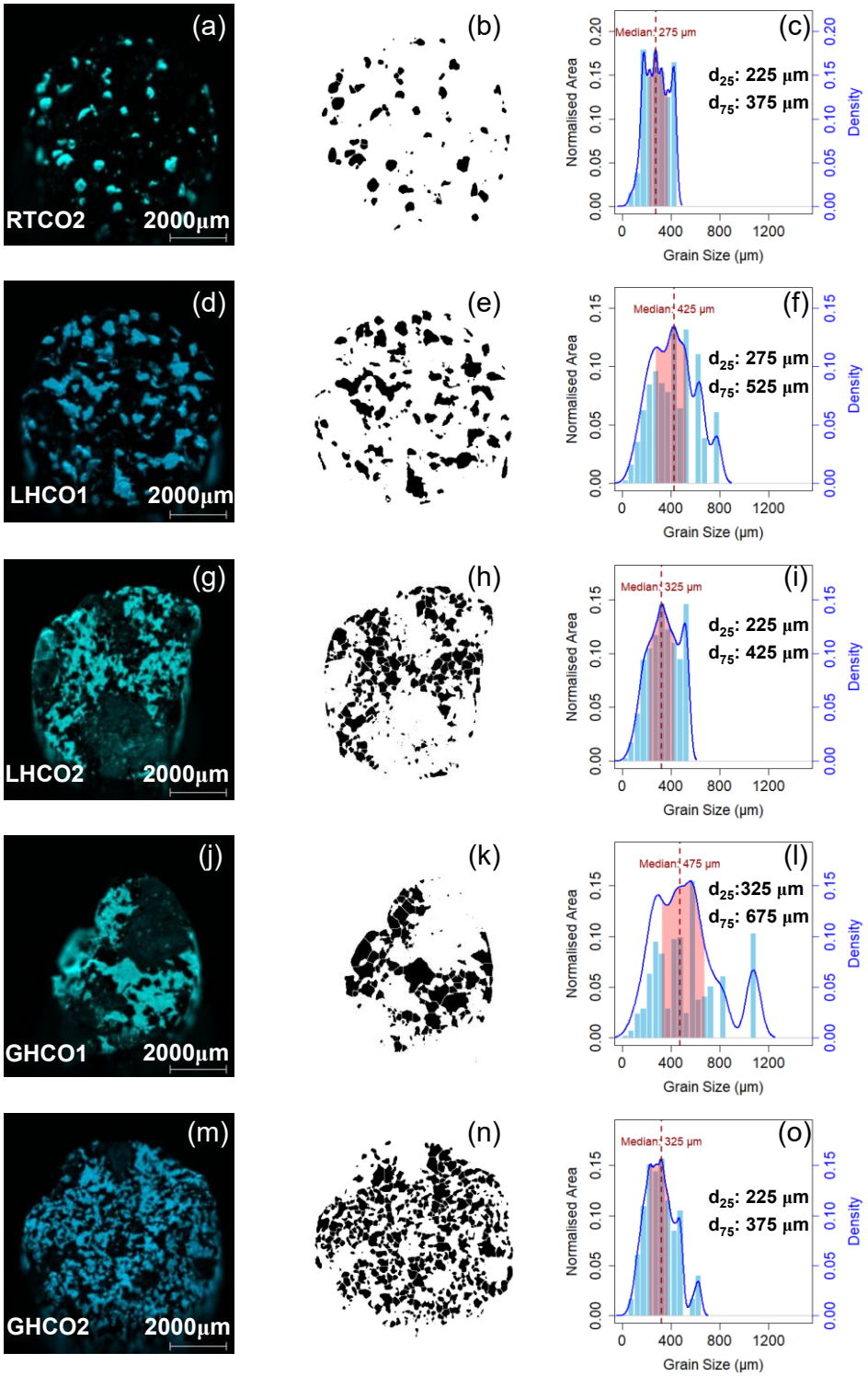

Fig. 5. *µ-XRF measurements and grain size distribution of K-rich feldspars in clast samples RTCO2 (a-c), LHCO1 (d-f), LHCO2 (g-i), GHCO1 (j-l) and GHCO2 (m-o). Left panels (a, d, g, j, m) represent the relative distribution of Potassium content within rock slices obtained from µ-XRF measurement with a spot size of 20 µm. Corresponding binary masks on the µ-XRF element maps are used to delineate individual grain boundaries and are shown in the middle panels (b, e, h, k, n), which are generated using graphical Imagej software analysis. Right panels (c, f, i, l, o) present the grain size distribution histograms along with kernel density estimates, illustrating the variation in k-feldspar grain sizes across the five slices. Grain sizes are plotted against normalised area (area covered by specific grain size interval are normalised to the total area covered by all grains present in the slice). An interquartile range (IQR) is highlighted as the red-shaded region within each histogram. The 25th percentile (d_{25}), 75th percentile (d_{75}) and the median (d_{50}) grain size are indicated within the IQR.*

burial bleaching event (Cossu *et al*., 2024; Sohbati *et al*., 2011). In this study, the bleaching front is identified based on the overall shape of the luminescence depth profile, characterised by a near-surface low-signal plateau followed by increasing L_n/T_n values with depth. Although the depth of the bleaching front varies among cores, all analysed cores from the Roethig and the Lingolsheim terrace clasts atleast exhibit evidence of a bleached near-surface domain with some of them exhibiting deeper bleaching fronts. This is interpreted to reflect differences in bleaching depth rather than the absence of pre-burial bleaching. Since model fitting of depth profiles has been avoided in current study, it is not possible to reliably distinguish well-bleached multiple slices within the near-surface domain. Therefore, the outermost slices from all investigated cores were used for age calculation to provide a consistent and unbiased representation of the pre-burial bleaching condition at the clast surface. Minor scatter within the bleaching front is attributed to lithological heterogeneity and measurement variability.

In RTCO1, the bleaching depth of IR_{50} signals varies notably among different cores of both its top and bottom surfaces. Core A (top) and core D (bottom) show deeper bleaching fronts, extending to ~7 mm from the surface, while shallower fronts (~5 mm from the surface) are present from the remaining top (B and C) and bottom (E and F) cores of the clast (**Fig. 6a**). The pIR_{110} signal bleaching fronts show less inter-core variability and extend to a depth of ~2 mm from both the top and bottom surface of RTCO1 (**Fig. 6b**). Unlike RTCO1, both the IR_{50} and pIR_{110} depth profiles yield consistent bleaching fronts across multiple cores of RTCO2 and the depth of bleaching fronts across multiple cores is observed at ~7 mm and ~3 mm respectively for IR_{50} and pIR_{110} signal profiles of RTCO2 (**Fig. 6e**, **6f**). The pIR_{170} and pIR_{225} depth profiles from both RTCO1 and 2 do not reveal a well-defined bleaching front at the surface of clast. However, the subsurface slice beneath the surface consistently exhibits higher pIR_{170} and pIR_{225} signal intensity compared to the shallowest slice, implying that the outermost surface layer is at least partially bleached. This pattern is consistent across multiple cores of RTCO1 and 2, indicating a limited but uniform bleaching effect in the high temperature pIR_{170} and pIR_{225} signals (**Fig. 6c**, **6d**, **6g** and **6h**).

Among the two clasts examined from the Lingolsheim terrace, LHCO1 exhibits well-bleached depth profiles for the IR_{50} and pIR_{110} signals measured within its multiple cores, with ~5 mm and ~3 mm bleaching fronts for IR_{50} and pIR_{110}, respectively (**Fig. 6i**, **6j**). The other clast, LHCO2, displays signal variability among its different cores, a ~4 mm deep IR_{50} bleaching front is observed for core C, while core A and B show shallower fronts, reaching <2 mm beneath the clast's surface (**Fig. 6m**). Uniformly shallow pIR_{110} bleaching fronts, restricted only to <2 mm into the surface, are observed for multiple cores of LHCO2 (**Fig. 6n**). Similar to RTCO1 and 2, no characteristic bleaching fronts are detected in the pIR_{170} and pIR_{225} depth profiles of either LHCO1 or LHCO2. However, the subsurface slices across multiple cores from both the clasts consistently exhibited higher pIR_{170} and pIR_{225} signals compared to their corresponding outermost slices, confirming that the clasts' surfaces are at least partially bleached (**Fig. 6k**, **6l**, **6o**, **6p**).

In contrast to the clasts from the Roethig and Lingolsheim terraces, the MET-pIRIR signals of the Griesheim terrace clasts (GHCO1 and 2) remain at saturation throughout the depth of the investigated cores. This is indicated by (i) L_n/T_n values consistently clustered near the saturation level, though with varying scatter between clasts (**Fig. 6q–6x**) and (ii) dose response curves indicating that saturation is already reached by the second shallowest slice in each core (in some cores, saturation is already observed even in the outermost slices). Although complete bleaching prior to burial could be considered as an alternative explanation to this scenario, the early onset of saturation in the dose response curves suggests that the MET-pIRIR signals are close to saturation rather than reflecting full resetting by sunlight exposure.

From the two modern day clasts (MODCO1 and 2), both the IR_{50} and pIR_{110} bleaching profiles reveal variable extents of pre-burial bleaching across the different cores. For each of them, the IR_{50} bleaching fronts extend to ~4 mm, while those for pIR_{110} signals are shallower (≤1 mm) (**Fig. S2a**, **S2b**, **S2e** and **S2f**). Bleaching fronts are restricted to <1 mm for pIR_{170} and pIR_{225} profiles across multiple cores for the modern clasts (**Fig. S2c**, **S2d**, **S2g** and **S2h**).

4.3. Fading Correction and Age Estimation

Table 3 summarizes the mean NLS ratios estimated utilizing three slices from each investigated clasts, following the approach outlined in Rades *et al*. (2018). For all clasts, the NLS ratios exhibit a systematic increment with increasing IR stimulation temperatures. Due to the impact of anomalous fading, the natural saturation of the feldspar grains within slices is consistently lower than the laboratory saturation, yielding NLS ratios <1 across the MET-pIRIR signals. Although, variability within NLS ratios is observed among the clasts from different terraces, ratios were internally consistent within the clasts from individual terrace. Clasts from the Roethig terrace exhibit NLS ratios of 0.40–0.45 for IR_{50}, 0.75 for pIR_{110}, 0.85–0.87 for pIR_{170} and 0.89–0.96 for pIR_{225} signal. For the Lingolsheim terrace, the clasts display NLS ratios of 0.38–0.46 for IR_{50}, 0.65–0.75 for pIR_{110}, 0.70–0.85 for pIR_{170} and 0.83–0.89 for pIR_{225} signal. In contrast, the clasts from the Griesheim terrace have overall higher NLS ratios, with 0.63–0.70 for IR_{50}, 0.83–0.90 for pIR_{110}, 0.92–0.96 for pIR_{170} and 0.98–0.99 for pIR_{225} signal (**Table 3**).

Luminescence ages from the clasts of the three terraces were calculated using the outermost surface slices from each core. The Central Age Model (CAM; Galbraith *et al*., 1999) was applied to obtain CAM D_e value for each IR

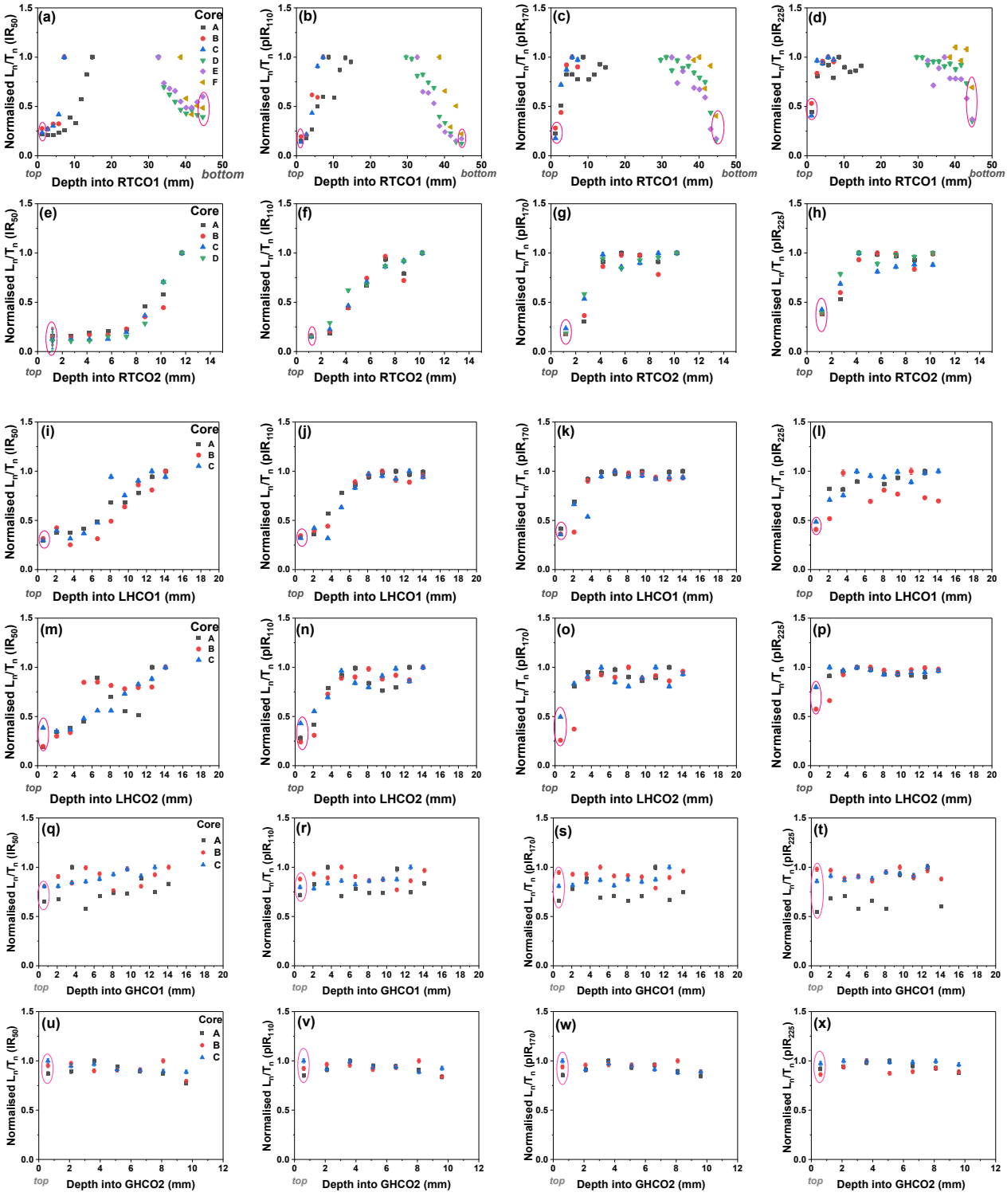

Fig. 6. *Depth profiles of normalised luminescence signals (L_n/T_n) from the investigated clasts of Roethig (a-d for RTCO1 and e-h for RTCO2), Lingolsheim terrace (i-l for LHCO1 and m-p for LHCO2) and Griesheim terrace (q-t for GHCO1 and u-x for GHCO2). Each data point represents the natural luminescence signal measured from individual rock slice at a specific depth of a single core, normalised to the maximum natural signal at each IR stimulation temperature obtained from the corresponding core. Error bars indicate the 1σ analytical uncertainty of the normalised L_n/T_n values. Luminescence signal variations into the depth of these six clasts are shown for IR_{50} (in panels a, e, i, m, q and u), for pIR_{110} (in panels b, f, j, n, r and v), for pIR_{170} (in panels c, g, k, o, s and w) and for pIR_{225} (in panels d, h, l, p, t and x). Surface slices are used for age calculation and are surrounded by red lines.*

stimulation temperatures. CAM MET-pIRIR D_e values exhibited overdispersion (OD) of ≤25%, except for the D_e values obtained for the pIR_{170} and pIR_{225} signals, recovered from the bottom cores of RTCO1, where a relatively higher OD (~54–56%) was obtained. **Table 3** summarizes the fading-uncorrected and fading-corrected CAM ages for the different MET-pIRIR signals for all clasts. Among the investigated clasts, bottom cores were successfully recovered only from RTCO1. However, no significant age offset was observed between the top and bottom surface of this clast.

The two clasts from the Roethig terrace (RTCO1 and 2) have fading-uncorrected ages ranging from ~12–13 ka, ~16–17 ka, ~22–31 ka and ~25–37 ka for the IR_{50}, pIR_{110}, pIR_{170} and pIR_{225} signals, respectively. Fading-corrected ages of the two clasts are systematically older, spanning ~27–33 ka for IR_{50}, ~22–23 ka for pIR_{110}, ~26–36 ka for pIR_{170} and ~28–39 ka for pIR_{225}.

For the Lingolsheim terrace, fading-uncorrected ages for LHCO1 and LHCO2 cluster at ~14–15 ka (IR_{50}), ~23–26 ka (pIR_{110}), ~22–28 ka (pIR_{170}) and ~22 ka (pIR_{225}). No pIR_{225} D_e value could be obtained for LHCO2, since the superficial slices produced natural D_e exceeding the laboratory saturation. Therefore, the pIR_{225} D_e values recovered only from the surface slices of LHCO1 were considered for pIR_{225} age estimation. After fading correction, ages for LHCO1 and 2 increase to ~39–40 ka for IR_{50}, ~35–41 ka for pIR_{110}, ~32–39 ka for pIR_{170} and ~26 ka for pIR_{225}.

Although the MET-pIRIR signals from GHCO1 and GHCO2 show saturation (**Fig. 6q-6x**), the D_e values from the surface slices of these two clasts are utilised to demonstrate that these clasts must be at least as old as the saturation limit of the signal, thus providing a minimum constraint on the timing of the terrace deposition. The clasts from the Griesheim terrace (GHCO1 and 2) probably record a much older episode of deposition. Fading-uncorrected ages of the two clasts range from ~120–149 ka (IR_{50}), ~161–236 ka (pIR_{110}) and ~217 ka (pIR_{170}), while the corresponding fading-corrected ages from them are ~190–213 ka, ~194–262 ka and ~236 ka. At high IR

Table 3. *Luminescence ages of the investigated clasts based on CAM D_e values estimated from the surface slices. Results are shown for all MET-pIRIR signals, with and without fading corrections. For each clast, the NLS ratio used for fading correction represents the mean value derived from three saturated slices taken from different cores. *Indicates that no D_e values could have been obtained from the rock slices of different cores for the corresponding clast, since the natural signals measured at higher IR stimulation temperatures (170°C and 225°C) approach saturation for the slices.*

Sample ID	Clast surface	Number of surface slices/ measured surface slices	IR stimulation temperature (°C)	CAM D_e (Gy)	OD (%)	CAM Age (ka)	NLS ratio	Fading corrected CAM age (ka)
RTCO1	Top	3/3	IR_{50}	35.2 ± 0.5	0	12.3 ± 0.7	0.40 ± 0.10	30.8 ± 7.9
		3/3	pIR_{110}	48.5 ± 0.7	0	16.9 ± 1.0	0.75 ± 0.14	22.6 ± 4.5
		3/3	pIR_{170}	85.4 ± 8.7	15	29.9 ± 3.5	0.87 ± 0.06	34.4 ± 4.7
		3/3	pIR_{225}	105.7 ± 9.7	15	37.1 ± 4.1	0.96 ± 0.03	38.6 ± 4.4
	Bottom	3/3	IR_{50}	38.1 ± 2.0	8.7	13.4 ± 1.1	0.40 ± 0.10	33.4 ± 8.8
		2/3	pIR_{110}	49.0 ± 5.3	15	17.1 ± 2.1	0.75 ± 0.14	22.8 ± 5.1
		3/3	pIR_{170}	88.7 ± 27.7	54	31.1 ± 9.9	0.87 ± 0.06	35.8 ± 11.6
		3/3	pIR_{225}	106 ± 32	56	37.3 ± 11.5	0.96 ± 0.03	38.8 ± 12.1
RTCO2	Top	4/4	IR_{50}	37.4 ± 1.1	5.1	12.4 ± 3.4	0.46 ± 0.05	26.9 ± 7.9
		4/4	pIR_{110}	51.8 ± 2.0	7.2	17.1 ± 4.7	0.75 ± 0.01	22.8 ± 6.2
		4/4	pIR_{170}	65.7 ± 7.0	22	22.3 ± 6.5	0.85 ± 0.03	26.2 ± 7.7
		4/4	pIR_{225}	75.6 ± 9.0	25	25.3 ± 7.5	0.89 ± 0.09	28.4 ± 8.9
LHCO1	Top	3/3	IR_{50}	92.1 ± 1.4	0	15.2 ± 1.1	0.38 ± 0.01	40.1 ± 3.1
		3/3	pIR_{110}	139 ± 3	0	23.0 ± 1.7	0.65 ± 0.01	35.4 ± 2.7
		3/3	pIR_{170}	167 ± 11	10	27.6 ± 2.7	0.70 ± 0.02	39.4 ± 4.0
		2/3	pIR_{225}	133 ± 6	0	21.9 ± 1.8	0.83 ± 0.04	26.4 ± 2.5
LHCO2	Top	2/3	IR_{50}	76.9 ± 2.2	3	14.8 ± 1.1	0.38 ± 0.01	38.8 ± 3.0
		2/3	pIR_{110}	138 ± 4	0	26.4 ± 1.9	0.65 ± 0.01	40.7 ± 3.1
		1/3	pIR_{170}	117 ± 3	--	22.4 ± 1.6	0.70 ± 0.02	32.1 ± 2.5
		0*/3	pIR_{225}	--	--	--	0.83 ± 0.04	--
GHCO1	Top	3/3	IR_{50}	592 ± 67	8	120 ± 15	0.63 ± 0.09	190 ± 36
		3/3	pIR_{110}	798 ± 68	2	161 ± 16	0.83 ± 0.13	194 ± 36
		2/3	pIR_{170}	1076 ± 26	0	217 ± 12	0.92 ± 0.08	236 ± 24
		0*/3	pIR_{225}	--	--	--	0.98 ± 0.01	--
GHCO2	Top	3/3	IR_{50}	750 ± 23	0	149 ± 13	0.70 ± 0.09	213 ± 33
		3/3	pIR_{110}	1185 ± 75	4	236 ± 24	0.90 ± 0.09	262 ± 38
		0*/3	pIR_{170}	--	--	--	0.96 ± 0.06	--
		0*/3	pIR_{225}	--	--	--	0.99 ± 0.01	--

stimulation temperatures (170 and 225°C), dose response curves from the superficial slices failed to yield reliable D_e values since the natural signals obtained exceed laboratory saturation. Therefore, surface slices from GHCO1 could not produce reliable pIR_{225} D_e values and the same applies for both pIR_{170} and pIR_{225} of sample GHCO2 (**Table 3**).

Besides, two modern clasts yield MET-pIRIR CAM D_e values or residual doses of ~1.5–2.3 Gy for IR_{50}, ~5.8–8.4 Gy for pIR_{110}, ~16.2–18.0 Gy for pIR_{170}, and ~23.7 Gy for the pIR_{225} signal. During D_e determination, surface slices from modern clasts often failed to meet the rejection criteria (recycling ratio within 10% and recuperation <10% of the natural dose). Therefore, D_e values from these slices were excluded and not discussed further. Following these criteria, only one surface slice from MODCO1 produced a reliable MET-pIRIR D_e and no pIR_{225} D_e could be obtained from MODCO2 (**Table S1**). Given that the two modern clasts exhibit granitic lithology comparable to one of the clasts obtained from the Roethig terrace (RTCO1), an equivalent environmental dose rate of ~3 Gy ka^{-1} — consistent with that derived for RTCO1 (**Table 2**) — was adopted to determine the approximate residual ages from the modern clasts. The resulting residual ages from the two analysed modern clasts are ~0.5–0.8 ka, ~1.9–2.8 ka, ~5.4–6.0 ka and ~7.9 ka for IR_{50}, pIR_{110}, pIR_{170} and pIR_{225} signal respectively (**Table S1**).

5. Discussion

5.1. Implications of Grain Size and K_{int} in Clast Dosimetry

To determine the dose rate from clasts, previous studies have used µ-XRF elemental mapping of feldspar grains (*e.g.* Rades *et al*., 2018; Yang *et al*., 2024) or microscopic observation on clast thin sections (*e.g.* Serra *et al*., 2025; Souza *et al*., 2021) to estimate either an average grain size or a minimum-maximum range of K-feldspar grain sizes. To better define the effective grain-size range, Ishii (2024) first reported the density distribution of K-feldspar grain sizes in rock slices and adopted the interval representing the densest 50% as a realistic estimate of grain size range. However, the relative area occupied by different grain-size groups within a rock slice was never accounted for in earlier studies. Grain size fractions covering larger areas within a slice are likely to contribute more to the overall IRSL signal obtained from the slice (Sellwood *et al*., 2022). In the current study, µ-XRF measurements of five rock slices reveal that the K-feldspar grains within a single slice distribute heterogeneously. They form clusters of both fine and coarse grains that are spatially close to each other. K-feldspar grain sizes identified from elemental mapping were plotted against normalized areas (*i.e.* the area covered by a given grain size interval relative to the total area of all grains in that slice) which resulted in non-unimodal distributions (**Fig. 5**). To define the dominant contributors to the signal, an effective range of grain sizes from each slice were represented using the interquartile interval (25^{th} to 75^{th} percentile).

Alongside, assuming a constant value for K_{int} can introduce systematic errors in clast dosimetry, which results in either over- or underestimated ages. Pure K-feldspar ($KAlSi_3O_8$) contains 14.0 wt% of K and natural feldspar grains exhibit a wide compositional range of 0–14 wt% K (Huntley and Baril, 1997). Therefore, for sediments, a generic value of 12.5 ± 0.5% is often assumed as K_{int} to calculate the environmental dose rate. However, such averages without clast-specific verification lead to inaccuracies (*e.g.* Ageby *et al*., 2023; Serra *et al*., 2025). In this study, microprobe analyses of clasts' thin sections confirmed the presence of abundant K-feldspar within them (**Table 2**). Moreover, the µ-XRF elemental mapping further revealed that K-feldspar is heterogeneously distributed across the rock slices, with most of the slice dominated by K-rich areas (**Fig. 5**). Minimum and maximum K concentrations determined from µ-XRF analyses using a 20 µm spot size across the slices for the Roethig, Lingolsheim and Griesheim terraces range from ~0.1 to 13%, ~0.2–1.4% to ~11–14%, and ~1.1–1.7% to ~12–15%, respectively. In addition, since gamma spectrometry already indicated high overall K% in the investigated clasts (**Table 2**), the maximum µ-XRF derived K values were more representative. A direct comparison between these maximum µ-XRF derived K% values and microprobe-derived K_{int} shows good agreement, overlapping within 1σ uncertainty (**Fig. 8**). Together, these parallel approaches allow a more robust estimation of K_{int} within the investigated clasts. Overall, the findings demonstrate consistent K_{int} within the clasts and variable K-feldspar grain size distribution among the rock slices, highlighting the possibility of uncertainties and inaccuracies associated with clast dosimetry when applying generalized assumptions of these factors to determine depositional ages from clasts. To quantify the magnitude of both of these parameters on the final depositional age of clasts, a quantitative assessment is conducted using representative clasts from this study. Comparison between commonly assumed K_{int} value (*i.e.* 12.5 ± 0.5%) and clast-specific µ-XRF-derived values indicates that a 1% increase in K_{int} results in ~3–6% decrease in calculated clast ages. The magnitude of this effect depends on the relative contribution of the internal dose rate to the total dose rate and may, therefore, vary among clasts.

In contrast, grain-size assumptions exert a substantially stronger influence in this regard. A 100 µm increase in the effective grain size results in an ~9–10% decrease in total dose rate, corresponding to an increase of ~10–11% in the finite age of a clast. The magnitude of this effect, however, likewise depends on the specific dosimetric context.

5.2. Resetting of High-Temperature IRSL signals in Rock Slices

A fundamental requirement for rock surface luminescence dating is that the luminescence signal in the first mm of clast depth is reset to near-zero level prior to burial (*e.g.* Freiesleben *et al*., 2015; Sohbati *et al*., 2015). The IR_{50} signal is known to bleach more rapidly under daylight exposure, resulting in well-bleached luminescence-depth profiles and low residual doses in rock slices (Freiesleben *et al*., 2023). In contrast, the higher temperature post-IRSL signals are generally more difficult to reset (Liu *et al*., 2022). In the current study, residual ages from modern day clasts are analyzed to evaluate the presence of the unbleachable signals at higher IR stimulation temperatures. The residual ages determined from two modern clasts indicate consistently higher values for pIR_{110} (~2–3 ka), pIR_{170} (~5–6 ka) and pIR_{225} (~8 ka) signals, while IR_{50} yielded residual ages below 1 ka (**Table S1**). These results confirm that daylight exposure during transportation of the clasts is often insufficient to completely reset the pIRIR signals (Yang *et al.*, 2024), resulting in shallower (<1 mm) or absent bleaching fronts for high temperature pIRIR depth profiles and, consequently, in higher residual ages. The residual ages of the modern clasts were calculated using the dose rate of RTCO2 on the basis of lithological similarity. Since the environmental dose rate of the modern clasts is not independently constrained, these residual ages represent an approximation. These residual ages are intended to assess the magnitude of inherited signal rather than to provide a precise correction. Given the uncertainty in the assumed dose rate for modern clasts, applying a residual correction could introduce additional systematic bias. Therefore, no correction was applied to the final depositional age estimates.The persistence of residual signals within modern clasts implies that clasts from the older terraces within similar fluvial settings likely retain unbleachable residual pIRIR signal components. This is evident from the absence of deep bleaching front in the analyzed clasts from the Roethig and Lingolsheim terraces (**Fig. 6**) and partly explains the overestimation of the clast ages compared to the independent age constraints (Marik *et al*., 2025), therefore highlighting the importance of measuring several clasts and cores to detect well-bleached profiles (Serra *et al*., 2025). Due to intra-core signal variability within the investigated clasts, it is not possible to reliably distinguish or select only "well-bleached" cores without introducing potential bias, as this could overrepresent locally well-bleached regions and may not reflect the overall bleaching condition of the clast surface. Therefore, the outermost slices from all investigated cores were included in the age calculation to provide a consistent and unbiased estimate of the depositional age. Minor variability among these slices is attributed to lithological heterogeneity and measurement scatter. However, the discrepancy between the fading-corrected clast ages obtained in the present study and the independent age controls (*ca.* 14–26 ka for the Roethig and *ca.* 6–7 ka for the Lingolsheim terrace–depending on the applied IR stimulation temperatures; **Fig. 7a** and **7b**) is considerably larger than the residual ages estimated from the modern clasts (*ca.* 1–5 ka). Moreover, even clasts and signals with well-bleached profiles (e.g IR_{50} signal of RTCO2; **Fig. 6e**) yield overestimated ages after applying fading corrections. This indicates that uncertainties in the fading correction procedure may represent an additional source of clast age overestimation (see section 5.3).

5.3. Assessing the Applicability of NLS Ratio for Age Calculation

Naturally saturated slices from a clast-interior can be used to calculate clast-specific NLS ratios, which are then used for fading correction (Rades *et al*., 2018). This approach is considered as more robust alternative to conventional g-value calculations, because it neither depends on extrapolating short-term to long-term laboratory fading measurements nor presumes a constant fading rate over geological timescales. Instead, the NLS ratio directly reflects the natural saturation behavior of each clast. As a result, deciphering saturation ratios has been adopted as a preferred fading correction method in recent studies associated with rock slices (Rades *et al*., 2018; Serra *et al*., 2025). Furthermore, the NLS ratio approach is particularly suitable for rock surface luminescence dating, as naturally saturated slices can be directly obtained from the interior of clasts and used for fading assessment. Such natural saturation conditions are generally not accessible in sand-sized sediment samples, where fading measurements rely on laboratory-derived g-values.

In the present study, NLS ratios have shown to increase consistently with the increment of IR stimulation temperatures across the investigated clasts (**Table 3**), confirming the greater stability of the higher temperature IRSL signals. For the Griesheim clasts this pattern is less clear, because of the limited number of slices suitable for pIRIR age determination (**Table 3**).

As discussed above, the application of fading corrections generally results in ages that are overestimated relative to the independent age control, even for clasts and profiles not affected by partial bleaching (*e.g.*, the IR_{50} signal of RTCO2; **Fig. 6e**). This suggests a potential overcorrection of the faded ages, possibly related to the selection of slices used for NLS estimation. The slices employed for NLS ratio determination were taken from the deeper portions of the clasts, where they were assumed to be unaffected by pre-burial sunlight exposure and therefore to represent saturation (so called saturation plateau). However, the IR_{50} and pIR_{110} luminescence depth profiles from the Roethig and Lingolsheim clasts show deep bleaching fronts, although no clear saturation plateau even at a greater depth within these clasts is observed (except for the pIR_{110} signal profile in LHCO1) (**Fig. 6**). Consequently, the IR_{50} and pIR_{110} natural saturation doses derived from

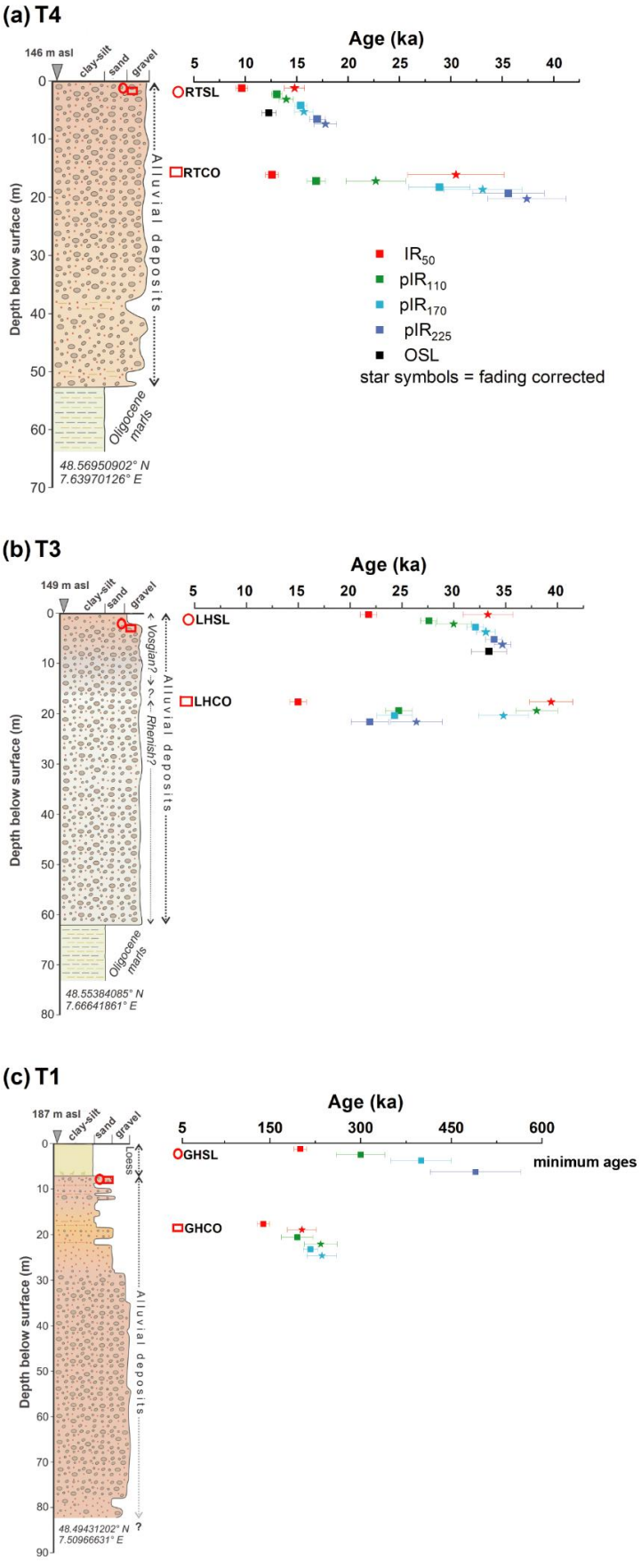

Fig. 7. *Stratigraphic logs of terrace deposits located in the vicinity of sampling site (a) T4, (b) T3 and (c) T1. The logs are drawn according to drilling reports available from the subsurface database of the French Geological Survey (https://infoterre.brgm.fr/viewer/MainTileForward.do). The different colours of the alluvial deposits are related to the different provenance of the sediment: greyish to light beige material points towards a Rhenish origin, whereas brownish to reddish material indicates a Vosgian origin. Red rectangles and circles within the stratigraphy mark the depth of clast and sand sample collection respectively. The panels in the right represent the estimated ages from sand samples (RTSL, LHSL, GHSL; Marik et al., 2025) and clasts (RTCO, LHCO, GHCO; current study) of each corresponding terrace. Each data point represents the age, calculated using central age model (CAM; Galbraith et al., 1999) of multiple sand or clast samples. For T1, no OSL ages could have been retrieved due to early signal saturation (Marik et al., 2025).*

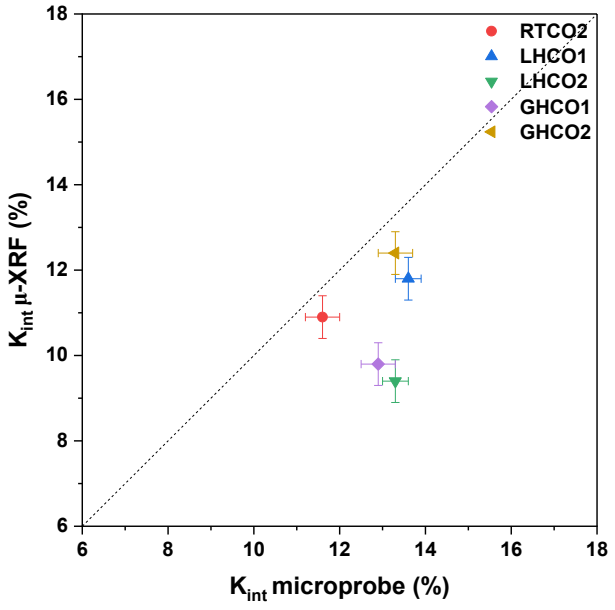

Fig. 8. *Comparison of internal potassium percentages obtained from microprobe analysis (x-axis) and μ-XRF analysis (y-axis) for the five clasts. For microprobe analysis, the error bars indicate standard 1σ error while a 5% relative uncertainty has been assumed as calibration and measurement error for μ-XRF analysis. All clasts plot below the 1:1 line because the microprobe measurements systematically yield higher K_{int} values than the point-based μ-XRF analyses. Since gamma spectrometry results from the investigated clasts indicated high overall K% in the investigated clasts (Table 2), the microprobe derived K_{int} values were considered more representative and were preferentially used for clasts' dosimetric calculations.*

these slices likely underestimate the true saturation level, leading to significantly overestimating the fading corrections (**Table 3**). Moreover, the degree to which saturation plateaus are expressed varies among signals and clasts. while some plateaus are well defined (*e.g.*, pIR_{225} in LHCO2), others display considerable scatter (*e.g.*, pIR_{225} in LHCO1 and pIR_{170} in LHCO2). This signal- and clast-specific variability in saturation plateau further complicates the reliable determination of NLS values and should be considered when interpreting the corrected ages.

Unlike the Roethig and the Lingolsheim terrace clasts, the MET-pIRIR depth profiles of the Griesheim terrace clasts exhibit long saturation plateau (**Fig. 6q-6x**). Therefore, the NLS ratio calculated from the central slices are considered reliable, as evidenced by the good agreement between the fading corrected MET-pIRIR CAM ages and the independent minimum age control (fading-uncorrected IR_{50} age; Marik *et al*., 2025; **Fig. 7c**).

These results emphasize the fact that, for the fading-correction approach based on the NLS ratio to yield accurate fading-corrected ages, it is essential to select rock slices from the internal saturation plateau within a clast-depth profile. Only when the slices reaching true saturation are targeted for determining the saturation ratio, the resulting fading-corrected ages precisely reflect the depositional ages from the clasts.

5.4. Comparison of Clast-Luminescence Chronology with Independent Age Control

As illustrated in section 4.3, clast-depositional ages in this study were determined using the MET-pIRIR D_e values derived from the outermost surface slices across multiple cores from individual clast. This strategy of depositional age estimation is different from the conventional model fitting procedure used in earlier rock surface dating studies (Ageby *et al*., 2021; Freiesleben *et al*., 2015; Moayed *et al*., 2023; Sohbati *et al*., 2015; Souza *et al*., 2021), where depositional ages of clasts were typically derived from curve-fitting of luminescence depth profiles. The model-based fitting parameters are hypothetical and may yield arbitrary values when the exposure time of a clast is unknown (Gliganic *et al*., 2024; Marik *et al*., 2024). In contrast, the approach undertaken in the present study aligns with the method adopted in comparable settings by Ishii *et al*. (2022). A luminescence depth profile with a characteristic sigmoidal shape indicates that the outermost slice from an investigating core should be completely reset by sunlight prior to burial. In the present study, a model-based approach to identify and utilise the full bleaching plateau was not applied, as such methods require assumptions about exposure duration and bleaching kinetics that are not well constrained for naturally transported clasts. Instead, depositional ages from clasts were exclusively derived using all the outermost slices of different cores. While multiple slices within a potential bleaching plateau may provide additional information, their use would require explicit modelling of both the bleaching profile and depth-dependent dose rate variations within the clast, which is beyond the scope of this study

Depositional ages obtained from the fluvial clasts of three different terraces are represented in **Fig. 7**, **9** and in **Table 3** together using the independent age control from Marik *et al*. (2025). To represent the luminescence ages for each terrace, a CAM of OSL and MET-pIRIR ages of the sandy samples from Marik *et al*. (2025) along with the CAM of MET-pIRIR ages for two clasts of corresponding terrace (current study) are presented by individual data point within **Fig. 7** and **9**.

For the Roethig terrace, the quartz OSL age obtained from the sandy deposits provides an independent age control of ~12.3 ± 0.7 ka (Marik *et al*., 2025). The MET-pIRIR ages derived from the clasts in this study range from ~13 to ~36 ka prior to fading correction and from ~23 to ~37 ka after fading correction. Both the fading-uncorrected and fading-corrected clast ages substantially overestimate the independent age control (**Fig. 7a**, **9a**). This age overestimation is likely attributable to the combined effects of the two factors— (1) presence of residual signals, resulting from incomplete bleaching of the high temperature MET-pIRIR signals (*i.e.* pIR_{110}, pIR_{170} and pIR_{225}) and (2) utilising the unsaturated rock slices from the centre of the clast-

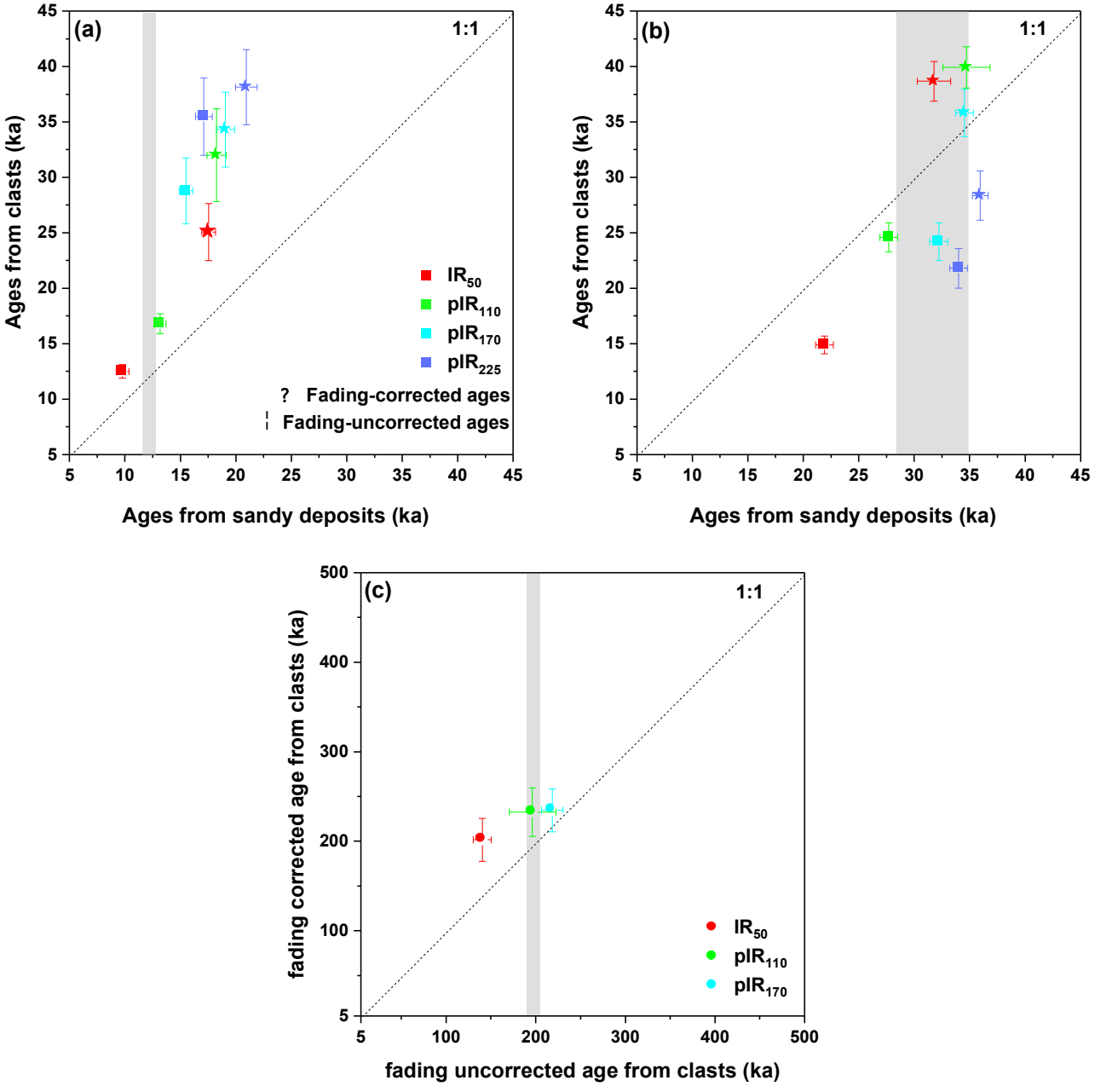

Fig. 9. *Comparison of clast-depositional ages with age control obtained on sandy deposits from (a) Roethig, (b) Lingolsheim terraces. Grey vertical bars indicate the OSL age ranges derived from sandy deposits within the corresponding terrace (previous study by Marik et al., 2025). Panel (c) indicates the comparison of fading-corrected and fading-uncorrected clast ages from the (c) Griesheim terrace. Grey vertical bar within panel (c) represents the minimum age control obtained from the Griesheim terrace sandy deposits (previous study by Marik et al., 2025).*

cores to calculate the NLS ratios. A further potential source of age overestimation may arise from the inclusion of slices that were not fully bleached prior to burial. Although the consistent presence of a near-surface low-signal domain across the analysed core profiles suggests that the outermost slices are likely well bleached (section 4.2), minor contributions from incompletely bleached slices into final age calculation cannot be excluded. For the Lingolsheim terrace, the quartz OSL age from the sandy deposits provides an independent age control of ~33.4 ± 1.7 ka (Marik *et al.*, 2025). The fading-uncorrected MET-pIRIR ages from the Lingolsheim clasts (~15 to ~28 ka) underestimate the independent age control. Following fading correction, these clasts yield MET-pIRIR ages of ~38–40 ka for IR_{50}, ~35–41 ka for pIR_{110}, and ~32–39 ka for pIR_{170}. While the IR_{50} and pIR_{110} ages tend to overestimate

the independent age control of the terrace, the pIR_{170} ages align within its uncertainty (**Fig. 7b** and **9b**). In contrast to the Roethig terrace clasts, where unbleachable residual pIRIR signals appear to be one of the principal causes of age overestimation, the overestimation observed in the unfaded IR_{50} and pIR_{110} ages from the Lingolsheim clasts is primarily attributed to overcorrection introduced during the fading correction procedure, where unsaturated central slices are used to calculate the NLS ratio and utilised to correct for fading. However, the fading-corrected pIR_{225} age (~26 ka) obtained from LHCO1 represents an exception, which underestimates the age control of the terrace. Although we cannot fully explain this deviation, it may reflect the fact that, since a limited number of slices (n = 2) from one sample (LHCO1) is used to derive the pIR_{225} age, it likely increased the uncertainty of the resulting age estimate.

From the Griesheim terrace, fading-uncorrected IR_{50} CAM ages (~200 ka) were considered to represent the minimum age of the terrace. No fading correction of the estimated MET-pIRIR ages was feasible due to field saturation of the feldspar signals (Marik *et al*., 2025) and the fading correction procedure failed to produce finite ages following Kars *et al*. (2008). Within the current study, fading-uncorrected CAM MET-pIRIR ages from the clasts of the Griesheim terrace exhibit ~139 ± 10 ka for IR_{50}, ~195 ± 26 ka for pIR_{110} and ~217 ± 12 ka for pIR_{170} signals. After fading correction, the MET-pIRIR CAM ages shift to ~203 ± 24 ka, ~234 ± 27 ka and ~236 ± 24 ka for IR_{50}, pIR_{110} and pIR_{170} signals respectively. Fading uncorrected and fading corrected CAM MET-pIRIR ages of the clasts together produce consistent depositional ages with the minimum age control established for the terrace (**Fig. 7c**, **9c**).

6. Conclusions

This methodological study highlights the critical importance of accurately determining the internal beta dose rate within the clasts to obtain reliable depositional ages using rock surface luminescence dating. The study discusses the uncertainties associated with the conventional assumption of K_{int} (typically presumed for homogeneous sandy deposits) and the approximation of K-feldspar grain size range in rock slices. A quantitative assessment presented in this study shows how the use of generalized assumptions of these two parameters can introduce deviations in a clast's depositional age, which underscores the importance of applying clast-specific constraints for deriving robust depositional ages from clasts. The study also emphasizes the need to carefully consider rock slices from clast-interiors when determining NLS ratios for reliable fading correction. Although, NLS ratios offer a more direct means of correcting for fading in rock slices compared to the conventional approach of g-value calculation, their effectiveness depends on proper selection of slices from clast centre. Results from this study clearly highlight that inclusion of unsaturated slices can produce overestimated fading-corrected ages. Furthermore, the results from modern clasts clearly indicate that residual signals persist in higher temperature pIRIR signals even within surficial slices, highlighting the importance of selecting luminescence-depth profiles that exhibit a well-defined bleaching front when applying rock surface dating to fluvial clasts, as an inadequate bleaching can lead to overestimated depositional ages, particularly in younger deposits. In summary, the findings from this study provide important methodological guidelines for improving the accuracy and precision associated with clast dosimetry which is essential to produce reliable depositional ages using rock surface luminescence dating.

Supplementary Material

Supplementary material containing additional figures and tables is available online at https://doi.org/10.20858/geochr/221620.

Author contribution

Frank Preusser and Madhurima Marik conceptualized and designed the project, which developed further under the supervision of Frank Preusser and Elena Serra. Gilles Rixhon carried out the logging and provided detailed lithological stratigraphy of the investigated terraces. Data interpretation and formal analysis have been done jointly by Madhurima Marik, Frank Preusser and Elena Serra. Madhurima Marik designed and carried out the experiments and wrote the initial draft of the manuscript. Figures were prepared by Madhurima Marik and Gilles Rixhon. Dominic Woelki and Stephan Opitz carried out the EMPA and energy-dispersive μ-XRF analyses, respectively, and contributed with software support, manuscript review and editing. Reviews and edits on the manuscript have been performed cumulatively by all the co-authors.

Acknowledgement

The authors are grateful to Dr. Lukas Gegg and Dr. Patrice Wuscher for actively helping in the fieldwork and with the sample collection process. The quarry managers of our studied areas are acknowledged for kindly providing us the access for sample collection. The authors also gratefully acknowledge the constructive comments of the anonymous reviewers, which helped to improve the manuscript.

Financial support

This study was financially supported by a scholarship from the German Academic Exchange Service (DAAD; grant no. 2100390601) granted to Madhurima Marik.

References

Ageby L, Angelucci DE, Brill D, Carrer F, Rades EF, Rethemeyer J, Brückner H and Klasen N, 2021. Rock surface IRSL dating of buried cobbles from an alpine dry-stone structure in Val di Sole, Italy. *Quaternary Geochronology* 66: 101212, DOI 10.1016/j.quageo.2021.101212.

Ageby L, Brill D, Angelucci DE, Brückner H and Klasen N, 2023. Investigating optical dating of carbonate-rich cobbles from a river terrace: A pilot study from the Mula Valley, Spain. *Radiation Measurements 166*: 106962, DOI 10.1016/j.radmeas.2023.106962.

Auclair M, Lamothe M and Huot S, 2003. Measurement of anomalous fading for feldspar IRSL using SAR. *Radiation Measurements* 37(4): 487–492, DOI 10.1016/S1350-4487(03)00018-0.

Baulig H, 1922. Questions de morphologie vosgienne et rhénane. *Annales de Géographie* 31(170): 132–154 (in French), DOI 10.3406/geo.1922.10257

Bøtter-Jensen L, Thomsen KJ and Jain M, 2010. Review of optically stimulated luminescence (OSL) instrumental developments for retrospective dosimetry. *Radiation Measurements* 45(3): 253–257, DOI 10.1016/j.radmeas.2009.11.030.

Castela P and Tricart J, 1958. Une coupe typique du cône de déjections nivo-périglaciaire de la Bruche : La carrière Zimmer à Lingolsheim. *Sciences Géologiques bulletins et mémoires 11*(2): 3–14 (in French), DOI 10.3406/sgeol.1958.1178.

Chamberlain EL and Wallinga J, 2019. Seeking enlightenment of fluvial sediment pathways by optically stimulated luminescence signal bleaching of river sediments and deltaic deposits. *Earth Surface Dynamics* 7(3): 723–736, DOI 10.5194/esurf-7-723-2019.

Cossu G, Sechi D, Sohbati R, Murray A, Pascucci V and Andreucci S, 2024. Luminescence dating of rock surfaces in challenging environments: The case of MIS5e gravelly transgressive lag deposit (Southern Sardinia, West Mediterranean Sea). *Quaternary Geochronology* 85, 101630, DOI 10.1016/j.quageo.2024.101630.

Degering D and Degering A, 2020. Change is the only constant—Time-dependent dose rates in luminescence dating. *Quaternary Geochronology* 58: 101074, DOI 10.1016/j.quageo.2020.101074.

Elkadi J, King GE, Lehmann B and Herman F, 2021. Reducing variability in OSL rock surface dating profiles. *Quaternary Geochronology* 64: 101169, DOI 10.1016/j.quageo.2021.101169.

Freiesleben T, Sohbati R, Murray A, Jain M, Al Khasawneh S, Hvidt S and Jakobsen B, 2015. Mathematical model quantifies multiple daylight exposure and burial events for rock surfaces using luminescence dating. *Radiation Measurements 81*: 16–22, DOI 10.1016/j.radmeas.2015.02.004.

Freiesleben TH, Thomsen KJ, Sellwood E, Liu J and Murray AS, 2023. Testing new kinetic models and calibration methods for Rock Surface Luminescence Exposure dating using controlled experiments. *Radiation Measurements 169*: 107033, DOI 10.1016/j.radmeas.2023.107033.

Fu X, Li B and Li SH, 2012. Testing a multi-step post-IR IRSL dating method using polymineral fine grains from Chinese loess. *Quaternary Geochronology* 10: 8–15, DOI 10.1016/j.quageo.2011.12.004.

Fu X and Li SH, 2013. A modified multi-elevated-temperature post-IR IRSL protocol for dating Holocene sediments using K-feldspar. *Quaternary Geochronology* 17: 44–54, DOI 10.1016/j.quageo.2013.02.004.

Galbraith RF, Roberts RG, Laslett GM, Yoshida H and Olley JM, 1999. Optical Dating of Single and Multiple Grains of Quartz from Jinmium Rock Shelter, Northern Australia: Part I, Experimental Design and Statistical Models. *Archaeometry* 41(2): 339–364, DOI 10.1111/j.1475-4754.1999.tb00987.x.

Gliganic LA, McDonald J and Meyer MC, 2024. Luminescence rock surface exposure and burial dating: A review of an innovative new method and its applications in archaeology. *Archaeological and Anthropological Sciences* 16(1): 17, DOI 10.1007/s12520-023-01915-0.

Huntley DJ and Baril MR, 1997. The K content of the K-feldspars being measured in optical dating or in thermoluminescence dating. *Ancient TL* 15(1): 11–13, DOI 10.26034/la.atl.1997.271.

Huntley DJ and Lamothe M, 2001. Ubiquity of anomalous fading in K-feldspars and the measurement and correction for it in optical dating. *Canadian Journal of Earth Sciences* 38(7): 1093–1106, DOI 10.1139/e01-013.

Ishii Y, Takahashi T and Ito K, 2022. Luminescence dating of cobbles from Pleistocene fluvial terrace deposits of the Ara River, Japan. *Quaternary Geochronology* 67: 101228, DOI 10.1016/j.quageo.2021.101228.

Ishii Y, 2024. IRSL and post-IR IRSL dating of multi-grains, single grains, and cobble surfaces to constrain fluvial responses to climate changes during the last glacial period in the Tokachi Plain, northern Japan. *Quaternary Geochronology* 79: 101486, DOI 10.1016/j.quageo.2023.101486.

Jain M, Murray AS and Botter-Jensen L, 2004. Optically stimulated luminescence dating: how significant is incomplete light exposure in fluvial environments?[Datation par luminescence stimulée optiquement: quelle signification en cas de blanchiment incomplet des sédiments fluviatiles?]. *Quaternaire* 15(1): 143–157, DOI 10.3406/quate.2004.1762.

Jautzy T, Schmitt L and Rixhon G, 2022. Historical geomorphological adjustments of an Upper Rhine sub-tributary over the two last centuries (Bruche River, France). *Géomorphologie: Relief, Processus, Environnement* 28(1): 53–72, DOI 10.4000/geomorphologie.16661.

Jenkins GTH, Duller GAT, Roberts HM, Chiverrell RC and Glasser NF, 2018. A new approach for luminescence dating glaciofluvial deposits—High precision optical dating of cobbles, *Quaternary Science Reviews* 192: 263–273, DOI 10.1016/j.quascirev.2018.05.036.

Kars RH, Wallinga J and Cohen KM, 2008. A new approach towards anomalous fading correction for feldspar IRSL dating—Tests on samples in field saturation. *Radiation Measurements* 43(2–6): 786–790, DOI 10.1016/j.radmeas.2008.01.021.

Kenworthy MK, Rittenour TM, Pierce JL, Sutfin NA and Sharp WD, 2014. Luminescence dating without sand lenses: An application of OSL to coarse-grained alluvial fan deposits of the Lost River Range, Idaho, USA. *Quaternary Geochronology* 23: 9–25, DOI 10.1016/j.quageo.2014.03.004.

Lautridou JP, Sommé J, Heim J, Puisségur JJ and Rousseau DD, 1985. La stratigraphie des loess et formations fluviatiles d'Achenheim (Alsace) : Nouvelles données bioclimatiques et corrélations avec les séquences pléistocènes de la France du Nord-Ouest. *Quaternaire* 22(2): 125–132, DOI 10.3406/quate.1985.1536.

Li B and Li SH, 2011. Luminescence dating of K-feldspar from sediments: A protocol without anomalous fading correction. *Quaternary Geochronology* 6(5): 468–479, DOI 10.1016/j.quageo.2011.05.001.

Liu J, Cui F, Murray AS, Sohbati R, Jain M, Gao H, Li W, Li C, Li P, Zhou T and Chen J, 2019. Resetting of the luminescence signal in modern riverbed cobbles along the course of the Shiyang River, China. *Quaternary Geochronology* 49: 184–190, DOI 10.1016/j.quageo.2018.04.004.

Liu Q, Chen J, Qin J, Yang H, Di N, Liu J and Zhang W, 2022. MET-post-IR IRSL luminescence dating of cobbles buried in fluvial terraces in the Northern Chinese Tian Shan. *Quaternary Geochronology* 72: 101351, DOI 10.1016/j.quageo.2022.101351.

Liu Q, Chen J, Qin J, Di N, Luo M, Yang H and Liu J, 2023. Zeroing of IRSL signals in cobbles surfaces from a modern river floodplain in the Manas river, Tian Shan. *Quaternary International* 672: 52–62, DOI 10.1016/j.quaint.2023.09.001.

Maire G, 1966. La Basse-Bruche : cône de piedmont et dynamique actuelle, PhD Thesis, Université de Strasbourg, Faculté de géographie et d'aménagement, 138 p. (in French).

Marik M, Serra E, Gegg L, Wölki D and Preusser F, 2024. Combined different luminescence dating approaches on fluvial gravel deposits from the southern upper Rhine graben. *Quaternary Geochronology* 82: 101536, DOI 10.1016/j.quageo.2024.101536.

Marik M, Serra E, Rixhon G and Preusser F, 2025. Luminescence dating of alluvial sediments from the Quaternary fan–terrace sequence of the lower Bruche valley, Upper Rhine Graben, France. *E&G Quaternary Science Journal* 74(2): 169–192, DOI 10.5194/egqsj-74-169-2025.

Moayed NK, Sohbati R, Murray AS, Rades EF, Fattahi M and Ruiz López JF, 2023. Rock surface luminescence dating of prehistoric rock art from central Iberia. *Archaeometry* 65(2): 319–334, DOI 10.1111/arcm.12826.

Ou XJ, Roberts HM and Duller GAT, 2022. Rapid assessment of beta dose variation inside cobbles, and implications for rock luminescence dating. *Quaternary Geochronology* 72: 101349, DOI 10.1016/j.quageo.2022.101349.

Prescott JR and Hutton JT, 1994. Cosmic ray contributions to dose rates for luminescence and ESR dating: large depths and long-term time variations. *Radiation measurements* 23(2–3): 497–500, DOI 10.1016/1350-4487(94)90086-8.

Preusser F, 1999. Luminescence dating of fluvial sediments and overbank deposits from Gossau, Switzerland: Fine grain dating. *Quaternary Science Reviews* 18(2): 217–222, DOI 10.1016/S0277-3791(98)00054-7.

Preusser F, Ramseyer K and Schlüchter C, 2006. Characterisation of low OSL intensity quartz from the New Zealand Alps. *Radiation Measurements* 41(7–8): 871–877, DOI 10.1016/j.radmeas.2006.04.019.

Preusser F, Degering D, Fülling A and Miocic J, 2023. Complex Dose Rate Calculations in Luminescence dating of lacustrine and palustrine sediments from Niederweningen, Northern Switzerland. *Geochronometria* 50*:* 28–49, DOI 10.2478/geochr-2023-0003.

Rades EF, Sohbati R, Lüthgens C, Jain M and Murray AS, 2018. First luminescence-depth profiles from boulders from moraine deposits: Insights into glaciation chronology and transport dynamics in Malta valley, Austria. *Radiation Measurements* 120: 281–289, DOI 10.1016/j.radmeas.2018.08.011.

Rades EF, Sohbati R, Alexanderson H, Jain M and Murray AS, 2024. Exploring the potential of rock surface luminescence from glacial sediments: Dating and transport history. *Boreas* 53(2): 227–242, DOI 10.1111/bor.12648.

Richter D, Woda C and Dornich K, 2020. A new quartz for γ-transfer calibration of radiation sources. *Geochronometria* 47(1): 23–34, DOI 10.2478/geochr-2020-0020.

Riedesel S and Autzen M, 2020. Beta and gamma dose rate attenuation in rocks and sediment. *Radiation Measurements* 133: 106295, DOI 10.1016/j.radmeas.2020.106295.

Riedesel S and Autzen M, 2023. calc_CobbleDoseRate(): calculate dose rate of slices in a spherical cobble. Function version 0.1.0, 2023. In: Kreutzer, S., Burow, C., Dietze, M., Fuchs, M.C., Schmidt, C., Fischer, M., Friedrich, J., Mercier, N., Philippe, A., Riedesel, S., Autzen, M., Mittelstrass, D., Gray, H.J., Galharret, J. (Eds.), Luminescence: Comprehensive Luminescence Dating Data Analysis. R package version 0.9.21. https://CRAN.R-project.org/package=Luminescence.

Roskosch J, Tsukamoto S and Frechen M, 2015. Luminescence dating of fluvial deposits from the Weser valley, Germany. *Geochronometria* 42: 126–138, DOI 10.1515/geochr-2015-0015.

Sellwood EL, Kook M and Jain M, 2022. A 2D imaging system for mapping luminescence-depth profiles for rock surface dating. *Radiation measurements* 150: 106697, DOI 10.1016/j.radmeas.2021.106697.

Serra E, Mueller D, Gegg L, Firla G, Piccoli F, Hergarten S, Margirier A and Preusser F, 2025. Combined single grain and cobble luminescence dating of poorly bleached glaciofluvial deposits from the Swiss Alpine foreland. *Quaternary Geochronology* 87: 101650, DOI 10.1016/j.quageo.2025.101650.

Singarayer JS and Bailey RM, 2004. Component-resolved bleaching spectra of quartz optically stimulated luminescence: preliminary results and implications for dating. *Radiation Measurements* 38(1): 111–118, DOI 10.1016/S1350-4487(03)00250-6.

Smedley RK, Duller GAT, Pearce NJG and Roberts HM, 2012. Determining the K-content of single-grains of feldspar for luminescence dating. *Radiation Measurements* 47(9): 790–796, DOI 10.1016/j.radmeas.2012.01.014.

Sohbati R, Murray AS, Jain M, Buylaert JP and Thomsen KJ, 2011. Investigating the resetting of OSL signals in rock surfaces. *Geochronometria 38*(3): 249–258, DOI 10.2478/s13386-011-0029-2.

Sohbati R, Murray AS, Porat N, Jain M and Avner U, 2015. Age of a prehistoric "Rodedian" cult site constrained by sediment and rock surface luminescence dating techniques. *Quaternary Geochronology* 30: 90–99, DOI 10.1016/j.quageo.2015.09.002.

Souza PE, Sohbati R, Murray AS, Clemmensen LB, Kroon A and Nielsen L, 2021. Optical dating of cobble surfaces determines the chronology of Holocene beach ridges in Greenland. *Boreas* 50(2): 606–618, DOI 10.1111/bor.12507.

Théobald N, 1955. Les alluvions anciennes au sud de la Bruche et aux environs d'Obernai (Bas-Rhin). *Sciences Géologiques, bulletins et mémoires* 8(1), 83–104 (in French), DOI 10.3406/sgeol.1955.1148.

Tissoux H, Rizza M, Aupart, C, Rixhon G, Valla PG, Boulay M, Lach P and Voinchet P, 2026. Exploring the relationships between Electron Spin Resonance (ESR)/ Luminescence (OSL/TL) properties and trace element composition from quartz in various bedrocks (Strengbach catchment, Vosges). *Geochronology* 8: 37–61, DOI 10.5194/gchron-8-37-2026.

Wallinga J, 2002. Optically stimulated luminescence dating of fluvial deposits: A review. *Boreas* 31(4): 303–322, DOI 10.1111/j.1502-3885.2002.tb01076.x.

Wintle AG, 1973. Anomalous fading of thermo-luminescence in mineral samples. *Nature* 245(5421): 143–144, DOI 10.1038/245143a0.

Wintle AG, 1977. Detailed study of a thermoluminescent mineral exhibiting anomalous fading. *Journal of Luminescence* 15(4): 385–393, DOI 10.1016/0022-2313(77)90037-0.

Wintle AG, 1997. Luminescence dating: Laboratory procedures and protocols. *Radiation Measurements* 27(5): 769–817, DOI 10.1016/S1350-4487(97)00220-5.

Wuscher P, 2021. Loess, alluvions et dépôts de pente du Fossé rhénan en Alsace de l'Eemien à l'Anthropocène : Approche pédosédimentaire, géomorphologie et chronostratigraphie. Phd thesis, Université de Strasbourg, 599 p.

Yang K, Ou X, Li Y, Jenkins G, Yao P, Tang D, Xu Y, Xie J, Zeng L and Liu X, 2024. Luminescence dating of cobbles buried in moraines from the source area of the Litang River (Konglongluo Valley), eastern Tibetan Plateau. *Quaternary Geochronology* 82: 101547, DOI 10.1016/j.quageo.2024.101547.